The University Of Queensland

AUSTRALIA

Looking for the Superfluid Fountain Effect in a Bose-Einstein Condensate

Callam Manning

Under the supervision of

Dr Tyler Neely

A thesis submitted to the University of Queensland

in partial fulfilment of the degree of Bachelor of Advanced Science

(Honours)

School of Mathematics and Physics

January 2020

Examiner's Copy

The work presented in this Thesis is, to the best of my knowledge and belief original, except as acknowledged in the text, and has not been submitted either in whole or in part, for a degree at this or any other university.

Callam Manning

Abstract

Superfluidity has been exhibited in numerous systems including Bose-Einstein condensates (BECs) and liquid helium. Superfluids have many characterising features with a particularly striking one being the superfluid fountain effect. This effect is characterised by the flow of a superfluid from one cooler reservoir to another hotter one. Since the superfluid fountain effect has yet to be observed in BECs, the aim of this project is to experimentally look for the superfluid fountain effect in a BEC confined within a 'dumbbell' configuration. This thesis focuses on the technical and analytical steps needed to look for the fountain effect in a BEC, including determining an appropriate heating method for the BEC and accurate measurement technique of its temperature. Heating techniques of 'bubbling' and 'shaking' were tested and found to be appropriate ways to have control over partially heating the BEC or turning it entirely into a thermal cloud. Another intermediate test was to measure the superfluid transport in the newly implemented optical 'box' potential that provides optimal isolation of the two dumbbell reservoirs. Despite promising preliminary results, the search for the superfluid fountain effect was eventually halted by the experiment's vacuum system failing after a number of other delays throughout the year. This thesis however makes progress towards looking for the superfluid fountain effect in a BEC to fill a gap in the demonstrations of a BEC as a superfluid and provides more knowledge as to how BECs transport when out of thermal equilibrium.

Acknowledgements

Thank you Tom for engaging with my project and discussing the heating methods with me.

Finally, thank you to everyone in the office who has shared in Honours year. You have made the experience all the more richer!

Contents

List of Figures

List of Tables

List of Acronyms

The following list is neither exhaustive nor exclusive, but may be helpful.

BEC . . . . Bose-Einstein condensate

DMD . . . . Digital micromirror device

MOT . . . . Magneto-optical trap

TOF . . . . Time of flight

1

Introduction

Bose-Einstein condensates (BECs) and liquid helium, when cooled below a transition temperature are superfluids, a fascinating quantum phenomena. Characteristic traits of superfluids include the ability to flow without dissipating energy below a critical velocity, and the appearance of vortices with quantized circulation. Perhaps the most striking feature of superfluids, and the feature which drives this research, is the *superfluid fountain effect*. This feature, which will be further explained in Section 2, is characterised by the flow of superfluid from cold to hot across a narrow channel connecting two reservoirs of superfluid.

The superfluid fountain effect was originally observed in superfluid helium, which is where superfluidity was first discovered [1]. There have since been a number of other superfluid systems realised. In this thesis, the one of interest is an ultra-cold atom system called a

Bose-Einstein condensate (BEC). Since their creation in 1995 [2, 3], there have been a number of tests of superfluidity analogous to the tests which have been performed with superfluid helium. These have included demonstrations of superfluid characteristics like existence of quantized vortices [4] and frictionless flow below a critical velocity [5]. However, the superfluid fountain effect has yet to be demonstrated in a BEC.

Although both BECs and superfluid helium are superfluid systems, the inter-particle interactions are much weaker in BECs [6]. As such, unlike superfluid helium, BECs are highly tuneable and controllable through optical and magnetic trapping techniques making them a highly controllable system for performing superfluid experiments. Fundamental research is often followed by the search for applications. Ultra-cold atomic systems, including BECs, are being explored as a new system for analogues of electronic device in 'atomtronics' research [7, 8] and even as heat engines [9–11]. As such, understanding the superfluid transport in different situations, especially subject to temperature and chemical potential gradients is then useful information which can be applied to developing these applications.

This work is motivated by the desire to look for these yet to be seen, but inherently novel thermomechanical properties that are manifest in superfluids and to better understand the particle transport in BECs when temperature differences are present. After some recent changes to the optical trapping of BECs in the University of Queensland (UQ) BEC lab, it has become an ideal system on which to perform this search. Using the optical trapping techniques available, the BEC will be confined within a 'dumbbell' pattern to mimic the two reservoirs connected by a narrow channel which is used in the superfluid helium experiment. Then, by preparing the two reservoirs at different temperatures, transport against the temperature gradient will be looked for.

In the next section, the superfluid fountain effect is investigated more deeply considering its origins with superfluid helium but its lack of observation thus far in BECs. The fundamentals of BECs and superfluid transport are discussed in Section 2 before looking at some prior research. Section 3 briefly outlines how BECs are created, trapped and imaged in the

lab at UQ with a focus on the new optical 'box' trap which creates a near uniform BEC and has the ability to easily remove any unwanted atoms from the trap. Section 4 contains the experimental process, results and analysis of the steps which were taken towards looking for the superfluid fountain effect in a BEC - namely heating of a BEC and the transport of the condensate in the new optical box trap. Some improvements to the existing code used to analyse the data is also presented. The final section summarises the extent of my research and provides an outlook for this work and the experiment including an addition to the coil set up.

2

Superfluid Systems and the Fountain Effect

2.1 Superfluid Helium Fountain Effect

Superfluidity was first realised in liquid He^4 in 1938 when it was cooled below its lambda point where it undergoes a phase transition (see Fig. 2.1) [1, 12]. A number of novel superfluid features have since been realised in superfluid helium. Some of these characteristic features include: the superfluid fountain effect (see Fig. 2.2 for description), friction-free flow below a critical velocity, high thermal conductivity and the presence of quantized vortices [16].

The superfluid fountain effect was discovered just months after superfluid helium was realised [13]. At first glance, this effect is somewhat counter-intuitive as the energy flow appears to be in the direction opposite to what the second law of thermodynamics would

dictate, although this is not the case. It was initially Tsiza in 1938 [14], and then Landau in 1941 [15] who more rigorously was able to explain this phenomena with the introduction of *the two-fluid model.*
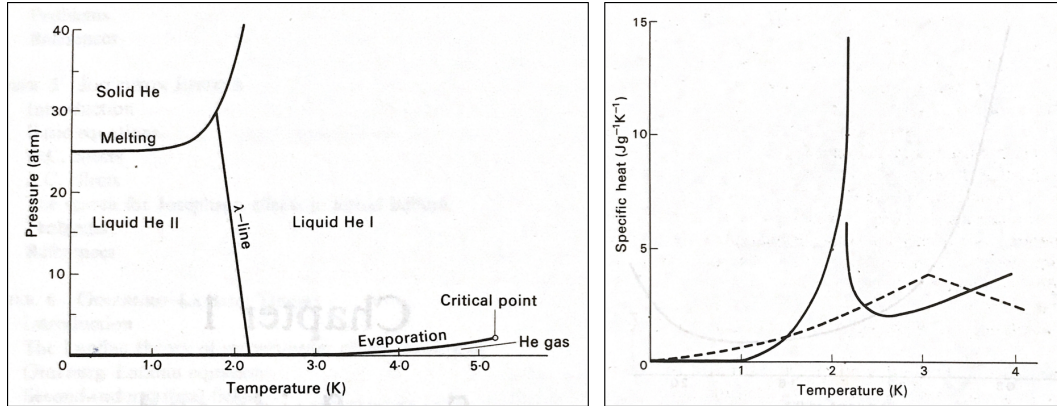
FIGURE 2.1: Images adapted from [16]. On the left is the phase diagram for He^4 where liquid He II is superfluid helium while He I is standard liquid helium. The transition from He I to He II occurs when liquid helium is cooled below the so-called 'lambda line' which is named for the shape of the graph on the right. The unbroken line is for He^4, while the broken line is for an ideal Bose-Einstein gas at the same density as the helium. For the homogenous BEC line, the cusp is at the critical temperature T_C. In the He II case, there is a discontinuity in the specific heat, whereas for a homogenous BEC, at the critical temperature there is no discontinuity. This however is not the case for a BEC in a 3D harmonic trap for example - in that case there is also a discontinuity similar to that of He II. [6]

The two-fluid model is a phenomenological model of superfluid helium in which the superfluid is composed of two components - a viscous 'normal' part which can transport heat (or entropy) and a 'superfluid' part which flows without viscosity and cannot transport heat. In the case of the superfluid helium fountain effect, as described in Fig. 2.2, there are two containers connected by a 'superleak' (the capillary). A superleak is a narrow hole which a viscous fluid could not flow through due to its surface tension. So, in the two-fluid model of superfluid helium, the normal part cannot flow through the superleak between the two containers, but the superfluid part can, as it has zero viscosity. Once one of the reservoirs is heated, a temperature imbalance is created in the system leaving the system out of thermal equilibrium. This temperature change also creates a chemical potential imbalance, but where the gradient points in the opposite direction to the temperature gradient (from thermodynamics, $\mu = -T(dS/dN)_{V,U}$). The chemical potential here is effectively the potential
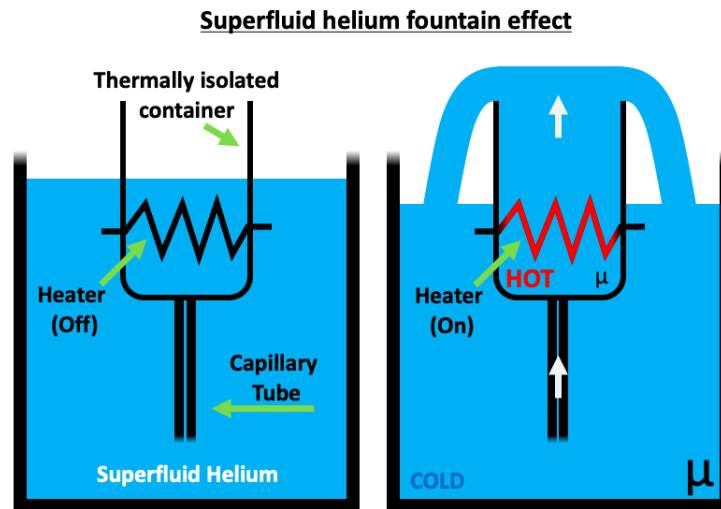
FIGURE 2.2: The superfluid helium fountain effect: The left frame is the system initially in equilibrium. There is a large reservoir of superfluid helium with a smaller and thermally isolated container connected by a superleak, depicted by a capillary. The right frame is the system after some heating of the superfluid helium in the smaller container. Subsequent to the heating, there is a temperature imbalance and a chemical potential imbalance (large μ indicates higher chemical potential than small μ). The result is superfluid helium flow from the larger, cooler reservoir into the smaller and hotter container of superfluid helium. The overflowing of the small container occurs from continuous heating and illustrates how the effect got its name.

energy per particle. This chemical potential imbalance leaves the system out of mechanical equilibrium. Naturally, the system wants to be in equilibrium, but in this case thermal equilibrium cannot be reached. As only the normal part of the superfluid can transport heat, it would need to flow between the heated and cooler reservoirs to reach equilibrium, but due to the superleak connecting them, this is not possible. In order for the system to move towards mechanical equilibrium where the chemical potential in both containers are equal, there needs to be a flow of particles from the cooler reservoir at higher chemical potential to the hotter reservoir at lower chemical potential. As increased particle number in a fixed volume and entropy also increases the chemical potential, it moves the system towards mechanical equilibrium. Hence, the superfluid component flows from the cooler reservoir to the hotter one creating the fountain effect. The results which characterises the fountain effect are a system stuck out of thermal equilibrium but moving towards mechanical equilibrium via the superfluid component flowing through the superleak from the cold to hot reservoir.

2.2   Bose-Einstein Condensates

A Bose-Einstein condensate (BEC) is another superfluid which, since its realisation in ultra-cold dilute quantum gases in 1995 [2, 3], has demonstrated many of the same properties of superfluidity as superfluid helium [4, 5, 17]. One property so far unobserved is the superfluid fountain effect, giving motivation to look for this phenomena in the novel system that is a BEC.

In order to create an atomic BEC, bosonic atoms must be cooled below a transition temperature (T_C) given approximately by,

$$T_C = C\frac{\hbar^2 n^{2/3}}{m k_B},$$
(2.1)

where C is a numerical factor ($C \approx 3.3$), $\hbar$ is $h/2\pi$ where h is Planck's constant, n is the number of particles per unit volume, m is the mass of the bosonic atom and k_B is Boltzmann's constant. Qualitatively, at T_C the de Broglie wavelengths ($\lambda = \sqrt{2\pi\hbar^2/(mk_BT)}$) of the atoms in question have a comparable length to their atomic spacing. As a result, the individual atomic wave functions merge into a macroscopic coherent wave function where individual atoms are now indistinguishable resulting in a BEC.

A more rigorous understanding of BECs can be achieved by realising bosons have integer spin and symmetric single-particle wave functions under particle exchange. As such, they are excused from the Pauli exclusion principle and many bosonic particles can occupy the same energy state. Since bosons obey Bose-Einstein statistics (Eq. 2.2), cooling these atoms increases the probability of finding a particle in the low energy states.

$$f_{BE} = \frac{1}{e^{(\epsilon-\mu)/k_BT} - 1},$$
(2.2)

where ϵ is the energy of the atom, μ is the chemical potential and T is the temperature. Once cooled below a transition temperature T_C, the atoms begin to preferentially occupy the lowest energy state. It is this mass congregation of atoms in the lowest energy state that is a

BEC. At absolute zero, a pure condensate can be achieved with all atoms in the ground state.

When BECs are experimentally created, the inability to reach absolute zero means that not all the atoms are in the ground state. As such, an experimental BEC is composed of two parts: the condensate and a thermal cloud. The thermal cloud is also composed of bosons, but at a higher energy state where the Bose-Einstein distribution is approximated to be the Boltzmann distribution:

$$f_B = e^{-(\epsilon - \mu)/k_B T}, \tag{2.3}$$

The relationship between the number of atoms in the condensate (N_0) and the total number of atoms in the system (N) is characterised by the condensate fraction:

$$\frac{N_0}{N} = 1 - \left(\frac{T}{T_C}\right)^\alpha, \tag{2.4}$$

where α is a factor which is dependent on the BEC trap (for example, in a 3D harmonic oscillator trap, $\alpha = 3$) [6].

In the superfluid helium fountain effect, the system is created with two physical containers separated by the capillary. To create an analogous situation for a BEC, optical traps are used (see Section 3) and the configuration must be different. In this thesis, we consider a 'dumbbell' configurations (Fig. 2.3) where one side can be heated and the channel between them acts as the superleak. Sections 2.3 and 2.4 consider superfluid transport in the dumbbell and similar configurations.

2.3   Superfluid Dynamics

Superfluidity is a quantum phenomena that is realised on a macroscopic scale, as can be seen by characteristics like vortices with quantized angular momentum. For the BEC case, another demonstration of their quantum nature is it is a macroscopically populated coherent
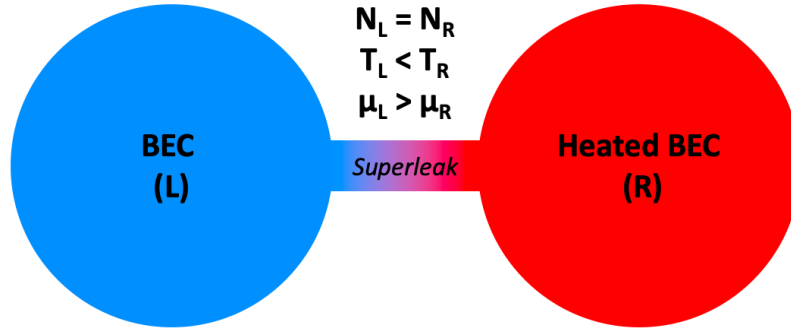
FIGURE 2.3: Ideal dumbbell configuration in which to trap a BEC and look for the superfluid fountain effect. The two reservoirs are connected by a channel which acts as a superleak. Both sides of the dumbbell have the same number of atoms but there is a temperature and chemical potential imbalance between the two side.

matter wave. Experiments have demonstrated this by showing matter-wave interference in BECs illustrating that BECs have a quantum phase, similar to the phase of a light wave [18]. As will be shown in section 2.3.1, this coherent quantum phase of the condensate drives the dynamics of a BEC. Some experimental examples of BEC transport are shown in section 2.3.2.

2.3.1 Gross-Pitaevskii equation

Since a BEC is a coherent matter wave, a mean-field wave function $\Psi(\mathbf{r}, t)$ can be used to approximate the condensate, where $\mathbf{r}$ is the spatial coordinate and t is time. To understand the dynamics of a pure condensate, a non-linear Schrodinger equation called the Gross-Pitaevskii equation (GPE) has been developed [6]. Equation 2.5 is the time-dependent GPE,

$$i\hbar\frac{\partial\Psi(\mathbf{r},t)}{\partial t} = \left[-\frac{\hbar^2}{2m}\nabla^2 + V(\mathbf{r},t) + g|\Psi(\mathbf{r},t)|^2\right]\Psi(\mathbf{r},t), \tag{2.5}$$

where $\Psi(\mathbf{r},t)$ is the many-body wave function, m is the particle's mass, $V(\mathbf{r},t)$ is the external potential and $g = 4\pi\hbar^2 a/m$ is the pre-factor to the non-linear term where a is the s-wave scattering length. Solving the GPE analytically becomes very difficult/impossible for anything but the most trivial cases, but it can be solved numerically. This also is quite

computationally expensive, but still some useful information about what drives BEC dynamics can be extracted from this equation without too much work. To see one relevant example of this, consider the hydrodynamic formulation of the GPE by writing the wave function in the Madelung transformation which satisfies both the time-dependent (Eq. 2.5) and time-independent versions of the GPE [19],

$$\Psi(\mathbf{r}, t) = \sqrt{n(\mathbf{r}, t)} e^{i\phi(\mathbf{r}, t)}, \tag{2.6}$$

where $n(\mathbf{r}, t)$ is the atomic number density and $\phi(\mathbf{r}, t)$ is the phase which is linearly dependent on time and the chemical potential of the system ($\phi = \mu t/\hbar$). Inserting the Madelung transformation (Eq. 2.6) into the probability current,

$$\mathbf{j}(\mathbf{r}, t) = \frac{i\hbar}{2m} \left(\Psi(\mathbf{r}, t) \nabla \Psi^*(\mathbf{r}, t) - \Psi^*(\mathbf{r}, t) \nabla \Psi(\mathbf{r}, t) \right), \tag{2.7}$$

gives,

$$\mathbf{j}(\mathbf{r}, t) = n(\mathbf{r}, t) \mathbf{v}(\mathbf{r}, t), \tag{2.8}$$

where $\mathbf{v}(\mathbf{r}, t) = n(\mathbf{r}, t) \hbar \nabla \phi / m$ is the velocity field and $\Psi^*(\mathbf{r}, t)$ is the complex conjugate of the wave function. The result shows that a velocity field, and hence superfluid flow, is created by a phase gradient. To experimentally create this phase gradient, one can create a chemical potential imbalance in the system, as this causes the phase to vary at different rates ($d\phi/dt = \mu/\hbar$, where μ is the chemical potential). Some demonstrations of this method driving transport are explored in Section 2.3.2.

Note that this result and the GPE are useful tools for a pure condensate, but for the superfluid fountain effect, there needs to be a temperature difference in the system. For a BEC, a temperature difference in the system corresponds to two different condensate fractions, so thermal atoms coming into play. In Section 2.4.2, a full numerical model of a potential experiment for the superfluid fountain effect in a BEC is considered, but here, the above

result from the GPE is to gain some intuition for what drives the superfluid flow in a BEC. This intuition is particularly useful in our case of interest of the dumbbell where a chemical potential and temperature difference can be created in the simple geometry of the system.

Thomas-Fermi approximation

An approximation that becomes briefly relevant for a model my results are compared to in Section 4.1 is the Thomas-Fermi approximation,

$$\left[V(\mathbf{r}) + g|\Psi(\mathbf{r})|^2\right]\Psi(\mathbf{r}) = \mu\Psi(\mathbf{r}), \tag{2.9}$$

which has the solution:

$$|\Psi(\mathbf{r})|^2 = \frac{\mu - V(\mathbf{r})}{g}, \tag{2.10}$$

when the right hand side is positive. Otherwise, the solution is $\Psi(\mathbf{r}) = 0$. For sufficiently large clouds where the kinetic energy term is small compared to other terms in the time-independent GPE (Eq. 2.11), it can be neglected to leave an accurate approximation of the condensate.

$$\mu\Psi(\mathbf{r}) = \left[-\frac{\hbar^2}{2m}\nabla^2 + V(\mathbf{r}) + g|\Psi(\mathbf{r})|^2\right]\Psi(\mathbf{r}). \tag{2.11}$$

In the Thomas-Fermi approximation, the energy it takes to add a particle to any point in the cloud is equal to the energy required at any other point. Near the surface of the condensate however, the kinetic energy becomes comparable to the interactions again. The distance this happens from the center of the cloud is called the Thomas-Fermi radius:

$$l_i = \sqrt{\frac{2\mu}{m\omega_i}}, \tag{2.12}$$

where i dictates the direction of interest (e.g. $i = x, y, z$) and ω_i is the trapping frequency in the i direction.

2.3.2   BEC transport between two reservoirs through a channel

There has been some research into BEC transport in a dumbbell configuration [20, 21] which can give some insight into what to expect from the condensate transport in my research.

In both of these examples, they consider condensate transport in the dumbbell when one reservoir is initially biased with a larger BEC population. This population imbalance results in a chemical potential imbalance between the two reservoirs (recall that for all other variables kept constant, chemical potential increases when atom number increases) which in turn drives the transport. Their experimental set ups use optical traps where blue-detuned light (from which atoms are repelled) creates the dumbbell to confine the BEC horizontally while the vertical confinement is done with a red-detuned sheet (atoms are attracted to regions of high intensity) creating a harmonic trap.

In the work by Eckel et al. [20], all the atoms initially were initially in one reservoir with a gate potential stopping any flow into the other reservoir. Once the gate is removed, the atoms flow through the channel into the other reservoir (Fig. 2.4 **a** shows in situ images of this process). This expansion and flow through the channel is due to the interaction mean-field energy changing. Once there is a BEC in the both reservoirs, the difference in phase (due to the atom number difference) drives the rate and direction of superfluid flow between the reservoirs. The results are depicted in Fig. 2.4 **b** and show two stages. The first stage is a dissipative stage where the flow is higher than the critical velocity of the superfluid resulting in the dissipation of energy and the atom number imbalance moves towards 0.5. The second stage is non-dissipative where the atom number imbalance oscillates about 0.5 indicating a non-equilibrium steady state. These oscillations are also and are an atomic analogue to the Josephson effect [22]. In their paper, Eckel et al. modelled the oscillations like an RLC circuit, depicted in the inset of Fig. 2.4, by solving three coupled differential equations.

The work done by Gauthier et al. [21] is similar but was performed to test a new model (lumped element acoustic) for the BEC transport in a dumbbell. This was done by performing a similar transport experiment to Eckel et al., but varying the channel width and length as well as varying the initial population bias. The results of Gauthier et al. are depicted in Fig. 2.5 and are qualitatively very similar to the results from Eckel et al. with an initial dissipative stage where the relative population tends towards a relative population which it oscillates about in the non-dissipative regime.
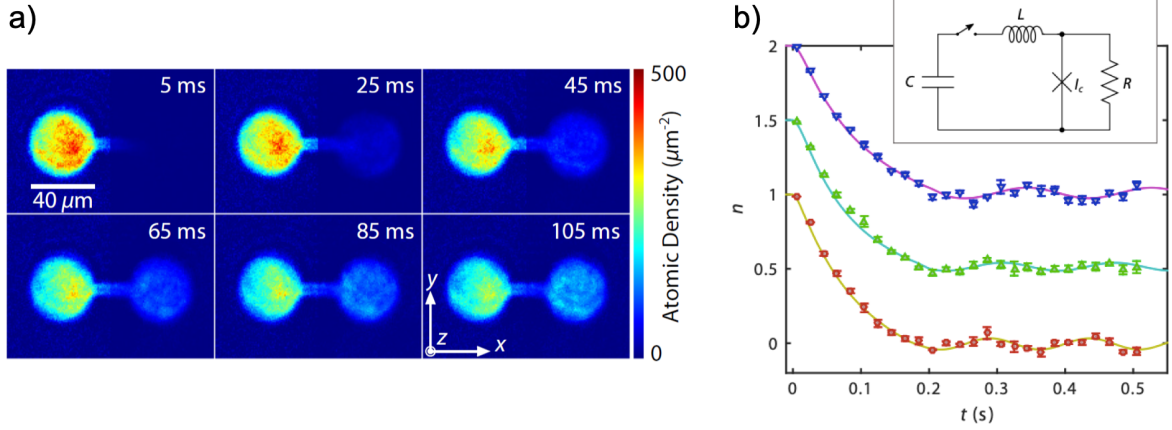
FIGURE 2.4: Images adapted from [20] . **a)** In situ images of evolution of the BEC in their dumbbell configuration **b)** Plot of normalised atom number imbalance ($n = \Delta N / N_e$, where ΔN is the number imbalance and N_e is the number of atoms in either reservoir at equilibrium) over time given three different one dimensional densities in the channel, each shifted by $n = 0.5$ for clarity. The 1D densities for the red, green and blue data are 790(25) μm^{-1}, 665(16) μm^{-1} and 599(17) μm^{-1} respectively .The inset is the analogous RLC electrical circuit which they model the transport on and is plotted with solid lines.
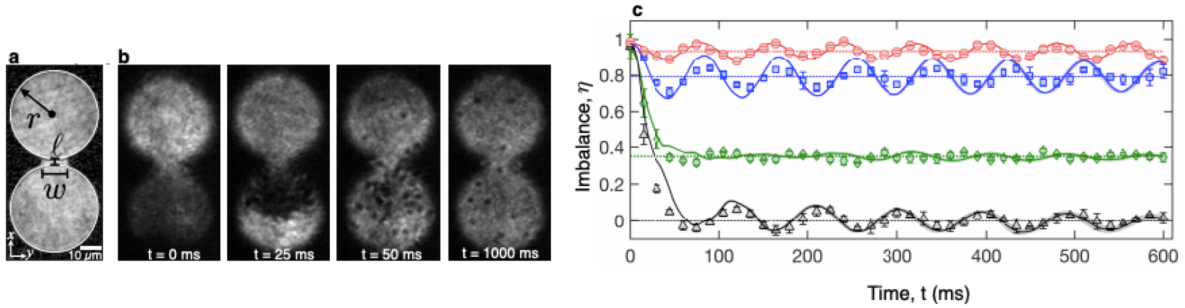
FIGURE 2.5: Images adapted from [21]. **a)** In situ image of a BEC in the dumbbell with annotations depicting channel length (l) and width (w) as well as reservoir radius (r). **b)** In situ images of the condensate dynamics over time for an initial population imbalance ($\eta = (N_1 - N_2)/(N_1 + N_2)$ where $N_{1,2}$ are measured populations in each reservoir) of $\eta = 0.96$. The dark dots are vortices illustrating the dissipation caused by the condensate flow through the channel with a large population imbalance. **c)** The dynamics of the population imbalance for different initial population imbalances - Red: $\eta = 0.03(1)$, Blue: $\eta = 0.18(1)$, Green: $\eta = 0.60(5)$, Black: $\eta = 0.96(1)$.

Gauthier et al. modelled the oscillations with as an acoustic Helmholtz oscillator and were able to make analogies to the existing circuit model, similar to that from Eckel et al. (see Fig. 2.6 for models). This model, in contrast to that of Eckel et al., allows for a

quantitatively accurate method to predict the dynamics of an atomic BEC in a dumbbell system, and as such, is directly relevant to my research. In fact, the Gauthier et al. work is performed on the same BEC apparatus that my research used, with the exception of the method of the trap providing the vertical confinement. The new trapping method is detailed in Section 3.4, but essentially it moving from trapping the BEC in a red-detuned sheet to between two blue-detuned sheets. G. Gauthier's paper thus provides an extremely useful reference to model the transport based on the parameters of the dumbbells and contrast the two trapping methods.
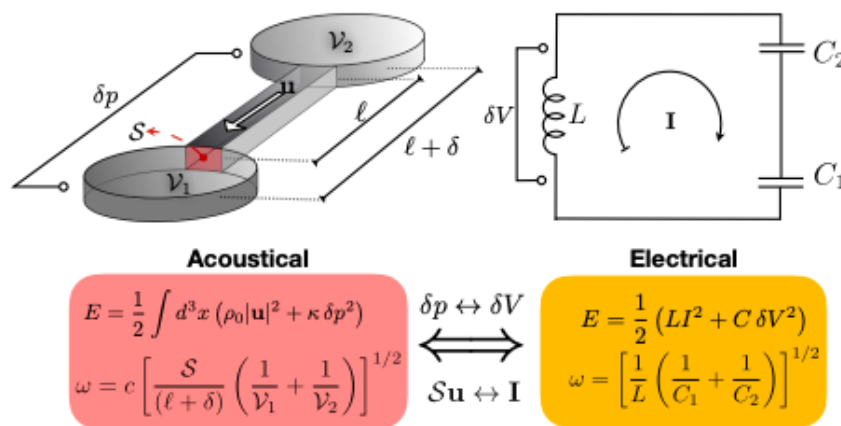
FIGURE 2.6: Acoustic model for superfluid flow in a Helmholtz resonator and corresponding LC circuit. In the acoustic model: ω is the oscillation frequency, c is the speed of sound in the superfluid, $\mathcal{S}$ is the channel's cross-sectional area, l is the channel's length, δ is the end correction, $\mathcal{V}$ is the volume of either reservoir, E is the exchange of energy between kinetic and potential energy, ρ_0 is the superfluid mass density at hydrostatic equilibrium, $\mathbf{u}$ is the velocity of the fluid between the reservoirs, κ is the compressibility of the fluid and $\delta\rho$ is the pressure changes associated with the superfluid velocity. And in the electrical model: L is the inductance, I is the current, C is the capacitance and δV is the change in voltage associated with the current.

2.4 The Fountain Effect in a BEC

One would expect that the results of looking for the SFE in an atomic BEC would not be exactly the same as that in the superfluid helium case because the same experiment cannot be carried out and they exist in different physical regimes. In the helium case, the interactions are strong and atomic collisions are relevant on the length scale of the experiment putting it

in the hydrodynamic regime. Whereas, for dilute atomic gases like BECs, the interactions are often weak with atomic collisions playing little-to-no part over the experiment which puts it in the mesoscopic particle transport regime. A few other significant differences are the number of atoms is much smaller in the BEC case and there is no simple way to keep the superfluid at a constant pressure in each reservoir for the BEC (i.e. the boundaries are set while in the helium case there is a fluid-air contact). All these differences mean that, from the outset, we can expect the results will look different. Nevertheless, one can still search for the three characterising features of the fountain effect: the system cannot reach thermal equilibrium, the system reaches (or at least moves towards) mechanical equilibrium and only the superfluid component travels through the superleak from the cold to hot reservoir.

Section 2.4.1 further explains the mesoscopic and hydrodynamic regimes and their importance in this work. There has been some numerical modelling considering what a superfluid fountain effect would look like in a BEC keeping in mind the above differences from the superfluid helium case in Section 2.4.2. Two separate groups via different method come to the same conclusion that the SFE could be experimentally realised in a BEC. In Section 2.4.3 we see that an analogue of the SFE has been seen experimentally in a different ultra-cold atom system: a unitary Fermi-gas. Later, Section 3.3 looks at a previous attempt of this experiment carried out here at UQ and considers why their results were inconclusive.

2.4.1 Hydrodynamic and mesoscopic particle transport Regimes

A system is said to be in the mesoscopic particle transport regime when the system is larger than an atom but where the particles in the system have a mean free path (l) on the same scale or larger than the system [6],

$$l = \frac{1}{n\sigma} \geq L, \tag{2.13}$$

where n is the particle density, L is the system dimension of interest, $\sigma = 8\pi a^2$ is the total scattering cross section and a is the s-wave scattering length. The mean free path (Eq. 2.13) is the typical distance a particle will travel before it collides with another particle. As such, in the mesoscopic regime, inter-particle collisions are infrequent so local thermal

equilibrium may be established on a non-negligible time scale within the experiment. Atomic BECs are typically weakly interacting dilute atomic gases with mean free paths which are typically longer than their system [6]. Section 3.1.1 performs a calculation demonstrating that the system in the UQ BEC is on the edge of the mesoscopic transport regime with the length of the system being about the same distance as the mean free path of a thermal atom.

If the mean free path is much less than the length of the system (i.e $l << L$), the system then enters the hydrodynamic regime. In this regime, inter-particle collisions are frequent (provided particles are not stationary) and thermalisation is faster. Experimentally, one can try to force the BEC into the hydrodynamic regime by increasing the number of atoms and increasing the size of the system through changing the geometry of the optical trap. For my experiment, the distinction between the hydrodynamic and mesoscopic regimes is important because the two fluid model was designed with the assumption that the system is hydrodynamic. Additionally, the different time scales for reaching local temperature equilibrium may also impact time scale on which any effects are measured.

2.4.2 Numerical models predicting fountain effect in BEC

In 2012, Karpiuk et al. [23] published a theory paper titled *Superfluid fountain effect in a Bose-Einsein condensate* where they propose an experiment which, their simulations show, should be able to demonstrate the superfluid fountain effect in a BEC. As this paper provides a method and results with an experimental apparatus similar to the one in UQ's BEC lab, the following paragraphs consider the paper more deeply than other journal articles referenced in this thesis.

In the modelling of Karpiuk et al., they consider a pure BEC at absolute zero (i.e. condensate fraction of 1) trapped harmonically with a blue-detuned barrier to split the trap into two sides. Then after preparing one side at a lower condensate fraction, but without changing the atom number, a channel is opened in the barrier allowing transport to occur. Their primary results from their simulations are depicted in Fig. 2.7, which is the plot we

would expect our experiment to produce if the fountain effect is present. Fig. 2.8 provides a qualitative depiction of these results.
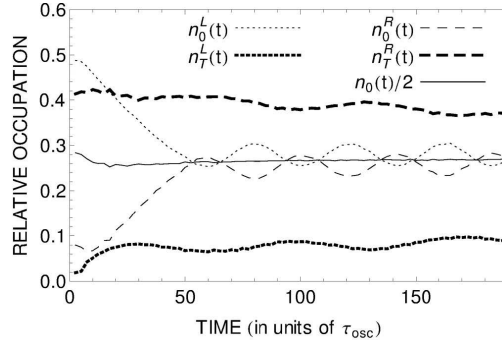
Figure 2.7: Image adapted from [23]. Relative occupation refers to occupation of the left (L) or right (R) reservoirs for the condensate (n_0) and thermal (n_T) parts. Initially, left reservoir is at 0K and the right reservoir has a condensate fraction of 0.2. The relative occupations of the thermal parts does not vary significantly indicating that most of the thermal cloud remains in their initial reservoir and doesn't flow through the channel, resulting in the system being unable to reach thermal equilibrium. The relative occupation of the condensate however quickly equilibrates before oscillating about half the relative occupation of the condensate.

The numerical modelling technique used to simulate the data in Fig. 2.7 is a classical field approximation which allows for the description of a dynamic system of condensates at non-zero temperatures. This method is essentially using the GPE but where the wave functions now incorporate information about the condensate (the lowest mode) and the thermal cloud (excited modes) by finding eigenmodes of the coarse-grained one-particle density matrix to give information about all the modes [23]. From these results, it becomes tempting to draw the analogy between the thermal and condensate and the normal and superfluid parts of the two-fluid model. Indeed, if you do this, you find the paper's results displayed the traits which characterise the superfluid fountain effect: the system reached a mechanical equilibrium in the system (they also have a plot of chemical potential to show this), the system did not reach thermal equilibrium (see Fig 2.7) and only the 'superfluid' part of the atomic cloud passed through the channel in from cold to hot.

Their simulations however showed that more than just the lowest mode (i.e. the condensate) flowed through the channel, as the first and second excited modes also flowed through (see Fig. 2.8). Yet they still draw an analogy to the two-fluid model, but call the lowest

three modes the 'superfluid' part and the rest the 'normal' part.
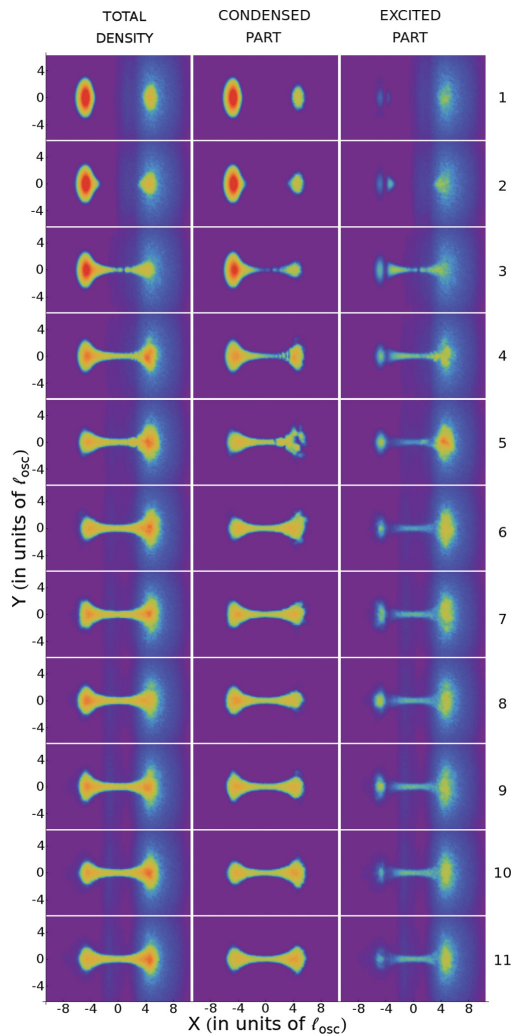
FIGURE 2.8: Image adapted from [23]. Simulation of evolution of Karpiuk et al.'s system over time for the total density, condensate and thermal components. The simulation evolves from the left reservoir being at 0K and the right reservoir having a condensate fraction of 0.2.

Although their overall results are very suggestive, they make a few important distinctions between their simulation results and the superfluid fountain effect as seen in superfluid helium. In the helium experiment, there is a large reservoir of the colder superfluid so there is a constant flow from cold to hot. However, in this paper's simulations, soon after the experiment begins, there are oscillations between the two sides, which can be seen in Fig 2.7. This is because there is no large reservoir of cold atoms, but instead an approximately equal number of atoms in each reservoir. Another distinction from the helium case is their

simulation is not in the hydrodynamic regime. BECs are generally (and are considered so in their simulations) a dilute gas and weakly interacting system, contrasting with superfluid helium which is a strongly interacting system. As such, Karpiuk et al. suggests that the two-fluid model with the thermal cloud as the 'normal' part and the condensate as the 'superfluid' part doesn't apply in their simulations. Nevertheless, the main features of the superfluid fountain effect are exhibited, mainly that thermal equilibrium isn't reached while the system moves towards mechanical equilibrium by the flow of the 'superfluid' through the channel.

A paper by Stringari et al. [24] is also of interest for this project because it agrees with the outcome of the work by Karpiuk el al. but also makes broader statements about when the superfluid fountain effect will be demonstrated in a BEC. This theoretical paper considers a homogeneous superfluid (e.g. BEC or He II) in a container of fixed volume with a partition creating two reservoirs, but the partition has a superleak in it. Initially both sides are in equilibrium, but then they heat one side and consider the particle flow driven by the need to reach chemical equilibrium. This paper highlights that this situation is different to the superfluid fountain effect in Helium II as the fixed volume means that any particle flow creates pressure. As such, they suggest that it is actually the pressure created by heating which stimulates the particle flow.

Their argument goes as follows: Let us define the differences in temperature, density and pressure between the two reservoirs (called left and right) as $\delta T = T_R - T_L$, $\delta n = n_R - n_L$ and $\delta p = p_R - p_L$ respectively. Since the system they consider can reach chemical equilibrium, we can enforce that $\mu_R - \mu_L = 0$. So we can rewrite δn and δp as

$$\delta n = \frac{\partial n}{\partial T}\Big|_\mu \delta T, \qquad \delta p = \frac{\partial p}{\partial T}\Big|_\mu \delta T. \tag{2.14}$$

The density derivative with respect to temperature can also be rewritten:

$$\frac{\partial n}{\partial T}\Big|_\mu = \frac{\partial n}{\partial \mu}\Big|_T \frac{\partial \mu}{\partial T}\Big|_n = -n^2 \kappa_T \frac{\partial \mu}{\partial T}\Big|_n, \tag{2.15}$$

where the first derivative becomes $-n^2 \kappa_T$ through some thermodynamic equation manipulations and κ_T is the isothermal compressibility. So, if we heat the container on the right, we

can see that the number of particles flows from cold to hot when $\delta n > 0$, so $\partial\mu/\partial T\big|_n$ must be negative. However, for a homogeneous BEC, they find that the $\partial\mu/\partial T\big|_n$ is positive so they expect flow opposite to that of a SFE. However, for a BEC in a harmonic potential, the derivative is negative due to the different mathematical form of the BEC's chemical potential and we expect to see the superfluid fountain effect.

Two important results should be highlighted from this paper: Stringari et al. agree with Karpiuk et al. that the superfluid fountain effect should be possible with BECs in a situation they describe. The caveat is that the trapping method of the BEC is a determining factor of whether the superfluid fountain effect is expected.

2.4.3   Superfluid fountain effect in a Fermi gas

Using a unitary Fermi gas, which is another superfluid system, an analogue to the superfluid fountain effect has been observed [25]. In the experiment by Husmann et al., they were able to separate a unitary Fermi gas into two reservoirs, heat one reservoir and then connect them using a quantum point contact (QPC). This is a situation analogous to the one used to see the superfluid fountain effect in helium where a hot and cold reservoir are connected by a superleak which is played by the QPC. Once the reservoirs were connected by the QPC, the particle and heat transportation through the QPC were measured.

Their results demonstrate a system which doesn't reach thermal equilibrium but does reach mechanical equilibrium, thus the system reached a non-equilibrium steady state suggestive of the superfluid fountain effect. Figure 2.9 depicts their primary results indicating the superfluid fountain effect were A) and C) indicate the system reaching a mechanical equilibrium through the flow of atoms from cold to hot and B) shows the system does not reach thermal equilibrium. In their measurements, Husmann et al. also measured a non-zero Seebeck coefficient which indicates that the atoms flowing from the cold to hot reservoir were carrying entropy. This violates the assumption in the two fluid model where the 'superfluid' part could not transport entropy (heat) between the reservoirs but only it could flow between

the reservoirs. As such, this demonstration of the superfluid fountain effect in an ultra-cold atomic system is an indication that the superfluid fountain effect can be seen even when the the situation is different to that described in the two fluid model. This demonstration suggests to us that the fountain effect may be observable in systems which do not satisfy all the assumptions made in the two-fluid model. For this thesis, the assumption which is failed is that the two-fluid model assumes the system is in the hydrodynamic regime, but this is not the case for our BEC system.
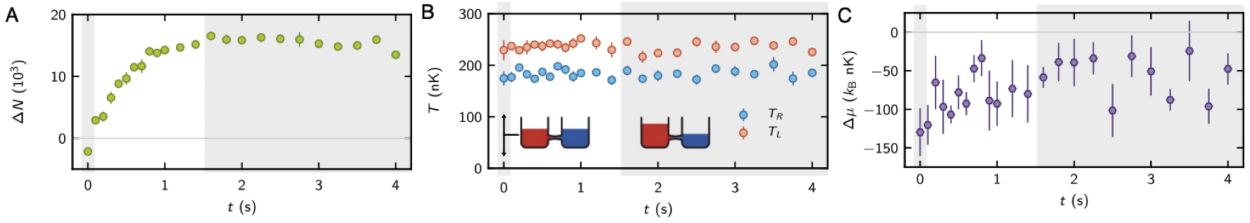
FIGURE 2.9: Image adapted from [25]. Results from after two reservoirs of a unitary Fermi gas at different temperatures were connected. A) Atomic population imbalance. B) Temperature of each reservoir. C) Calculated chemical potential imbalance.

There are a number of differences between the experiment of Husmann et al. and the one I intend to do in this thesis. Firstly, their system comprises of fermions which obey different statistics to bosons and obey the Pauli exclusion principle. One consequence of this is that their system is well inside the hydrodynamic regime whereas our BECs are not. Another difference is that in the BEC system, there are two different components which obey different statistics (the thermal cloud and the condensate) whereas there is no two component nature in this Fermi gas their system. As such, in looking for the superfluid fountain effect in a BEC, we can learn more about the thermomechanical properties of a superfluid in the mesoscopic particle transport regime, a situation not explored in the unitary Fermi gas.

3

Experimental Apparatus

This section briefly summarises the trapping (Section 3.1 and 3.1.2) and creation (Section 3.1.2) of BECs as well as the imaging techniques used for data analysis (Section 3.2). For a more comprehensive description of these aspects of the apparatus, see Refs. [26, 27]. Section 3.3 reviews a previous attempt to see the superfluid fountain effect in a BEC at UQ. Section 3.4 describes the addition of the 'green sheet' to the apparatus which was not included in those references or the previous attempt but is a vital component of the optical box trap created in conjunction with the DMD.

3.1   BEC Creation and Trapping Prior to Optical Box Trap

In order to perform an experiment on a BEC, one needs to be able to trap and manipulate it as desired. The experiment in the UQ BEC lab uses both magnetic and optical methods to trap and control the BEC. Here I will just focus on the optical trapping methods confining the atoms horizontally and vertically. The horizontal confinement is achieved through the use of blue-detuned light (which repels the atoms) controlled by a digital micro-mirror device (DMD), which is explained in Section 3.1.1. The vertical confinement, up until mid 2019, was limited to a red-detuned 1064nm beam tightly focussed in the vertical direction. This trap, called the 'red sheet', is a near-harmonic potential where the atoms are attracted to regions of high intensity. This year, I assisted a masters student named Maarten Christenhusz to implement and characterise an optical box trap [28], which is described in section 3.4. It is an important addition to the experiment in the search for the superfluid fountain effect as it removes some of the issues when the fountain effect experiment was previously attempted (see Section 3.3).

3.1.1   Digital micro-mirror device

For a more extensive explanation of the DMD as an optical method of horizontally confining BECs, see Refs. [26, 27]. The device itself is an array of mirrors (1200 × 19200 mirrors, each with a pitch of 10.8μm), each of which can be individually turned 'on' or 'off' dictating whether the 532nm blue-detuned light is reflected and subsequently imaged onto the atom plane. As such, arbitrary patterns can be created, including the pattern of interest in this research - the 'dumbbell'. The mirrors can also be controlled while the BEC is in-trap allowing for the dynamic manipulation of the potential. This is utilised to heat the BEC (see Section 4.2).

In the experiments performed in Section 4, the maximum size of the DMD pattern on the atom plane is about (210×130) μm. This, in conjunction with the density of the atom cloud,

places the system on the edge of the mesoscopic particle-transport regime. As mentioned in Section 2, this is one difference from the superfluid helium case which means that the two-fluid model may not be directly applicable.

As a demonstration, this is a calculation illustrating mesoscopic size of system: The UQ BEC lab can routinely create a BEC with a condensate fraction of 0.85 using 4×10^6 atoms. It can be confined horizontally in a 100 μm diameter disk created with the DMD, and vertically by the red sheet creating a 6 μm thick cloud. So, there are $N_{Th} = 0.15 \times 4 \times 10^6 = 6 \times 10^5$ thermal atoms trapped in a volume of $V = \pi \times (100/2)^2 \times 6 = 4.7 \times 10^4$ μm^3. The mean free path (l) of the thermal cloud is then $l = 1/(n\sigma) = (V/N_{Th}) \times 1/(8\pi a^2)$, where $n = N_{Th}/V$ is the density of the thermal cloud, σ is the total scattering cross section and $a = 99a_0$ is the s-wave scattering length for rubidium 87 atoms with $a_0 = 5.3 \times 10^{-11}$ m being the Bohr radius. The resulting mean free path of a thermal atom in such a situation is $l = 113$ μm. This is slightly longer than the length of the disc in which the atoms are trapped putting the atoms in the mesoscopic particle-transport regime.

This year, new optical fibres (LMA-PM-10 from NKT Photonics) have replaced the previous fibres which are used to couple light from one part of the DMD path to another. These new fibres have an increased numerical aperture (NA) which leads to the fibres being more easily coupled to the light. This means that the optical power reaching the DMD will be more stable as the coupling is less sensitive to drifts of the laser.

3.1.2 BEC creation

The research presented in this thesis uses the BEC lab at UQ which can create a BEC of $3 - 4 \times 10^6$ ^{87}Rb atoms in the $5^2\text{S}_{1/2}|F = 1, m_F = -1\rangle$ state with a condensate fraction $> 85\%$. What follows is a summary of how BECs are created on this experiment, however a more detailed explanation can be found in Ref. [27].
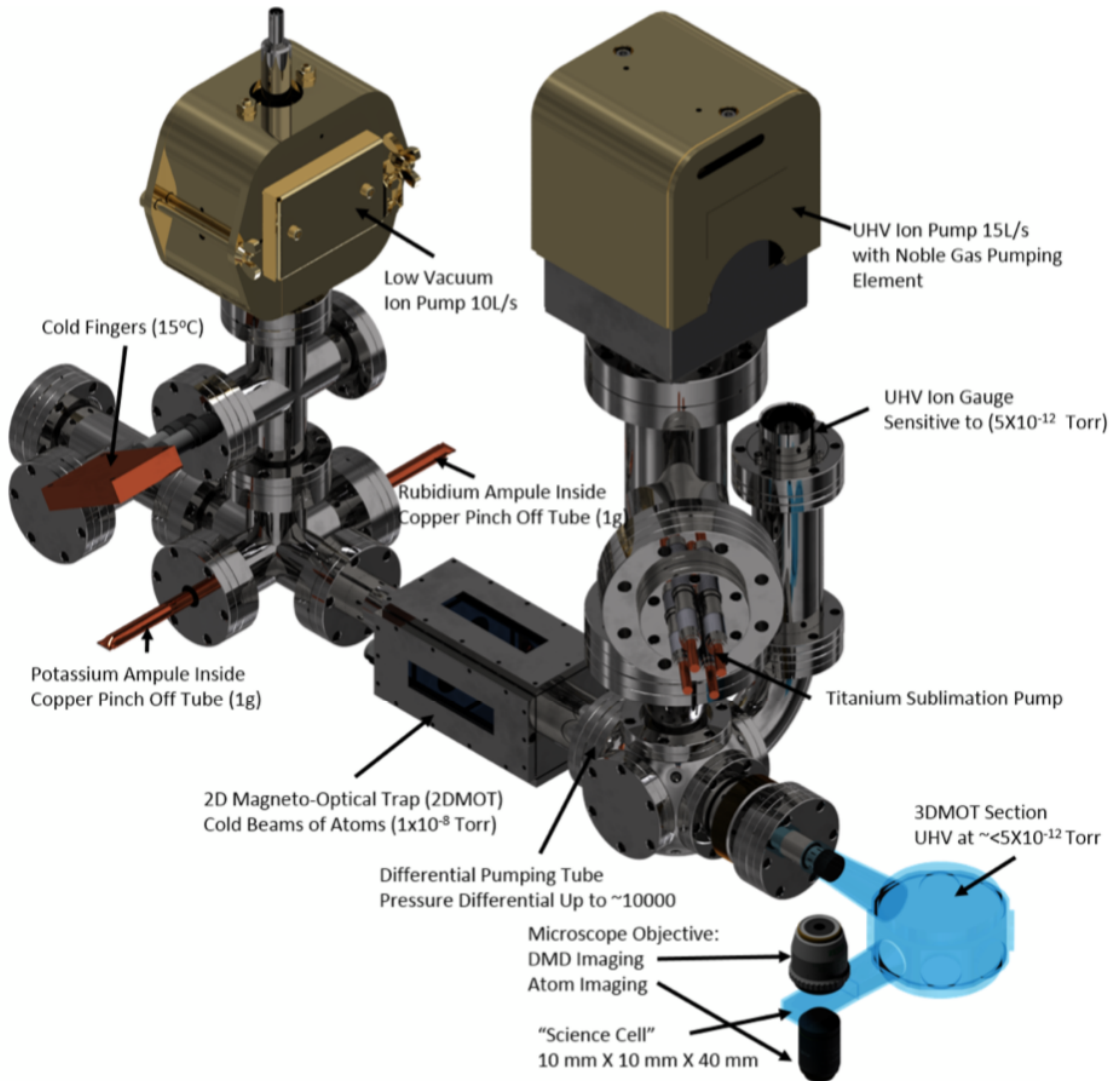
FIGURE 3.1: Vacuum system in UQ's BEC laboratory, adapted from [27].

The first cooling step is Doppler cooling in a magneto-optical trap (MOT). Doppler cooling essentially reduces the motion of an atom by creating an effective friction force through absorption and re-emission of photons. Consider an atom travelling along the light path of two counter-propagating laser beams which are red-detuned from the atoms transition (i.e. the laser frequency is lower than that of the atoms transition frequency). The atom sees the oncoming light at a frequency closer to its transition frequency than the trailing light, thus it absorbs more readily from the oncoming beam resulting in a net force opposing its motion. The re-emission of the photons is isotropic, so has a net zero effect on the atom's

motion, but it causes it to go on a random walk. A magnetic field is applied in a MOT to contain the atoms within the laser beams.

In the experiment, atoms are first cooled in a 2DMOT (rectangular prism in between low vacuum ion pump and UHV ion pump in Fig. 3.1) on the high vacuum side before being moved to the ultra-high vacuum 3DMOT where they are cooled to about 100μK in the glass octagon. The density of the cloud is then increased through a compression step. The $5^2\mathrm{S}_{1/2}|F = 1, m_F = -1\rangle$ state of the rubidium atoms seeks low magnetic fields, so this allows for the transfer then of such atoms in the cloud from the 3DMOT to the science cell using magnetic trapping techniques.

In the science cell, seen to the lower left of the octagon in Fig. 3.1, the cooling continues through microwave evaporation. This process changes the state of high energy atoms from the $|F = 1, m_F = -1\rangle$ state, which is a magnetically trappable state, to $|F = 2, m_F = -1\rangle$ which is not a magnetically trappable state, thus these atoms are expelled from the trap. The atoms are then transferred into a red-detuned 1064nm optical dipole trap where optical evaporation is performed from their initial temperature subsequent to microwave evaporation of about 4.5μK. As the rubidium atoms are attracted to regions of high intensity in a red-detuned optical trap, the evaporation technique is simply lowering the optical power of the trap, resulting in a lower trap depth and higher energy particles escaping and an overall decrease in kinetic energy. The result is a cloud of about 450nK, just above the BEC transition temperature. The final step is transferring the atoms into a red-detuned 1064nm beam (called the 'red sheet' trap) where the DMD is also turned on and the magnetic trap is also turned off. Here, more optical evaporation is performed until the BEC is created. Here, the BEC is confined vertically by the red sheet, which is focussed in that direction, while it is confined confined horizontally by the DMD.

The final step is to transfer the BEC to the newly implemented box trap (Section 3.4), by ramping down the power in the red sheet while ramping up the green sheet power.

3.2   Imaging

Once the experiment is run, in order to retrieve the results to be analysed, the BEC is imaged. Two destructive processes are used on the UQ experiment: absorption imaging and Faraday imaging. Below briefly summarises the method by which these images are acquired but more information can be found in Ref. [27].

Absorption imaging is achieved by taking three images - one without any light or atoms, one with just the imaging light and then one with imaging light and atoms. The imaging light is resonant and thus, when shone onto the atoms it is scattered. As such, the image taken with the atoms has a shadow produced by the atoms. The attenuation of the light by the atoms is given by the Beer-Lambert law, from which the column density of an image can be obtained, and hence the atomic population. In the images presented however, the optical density (OD - see Eq. 3.1) is the scale which is used and it is directly proportional to the atomic population. This imaging technique is used to image horizontally, and can be used to image vertically as well.

$$OD = \ln\left[\frac{I_0(x,y)}{I_A(x,y)}\right], \qquad\qquad (3.1)$$

where $I_0(x,y)$ is the initial imaging light intensity profile and $I_A(x,y)$ is the attenuated light intensity profile.

Faraday imaging is the other technique used for vertical imaging of the BEC in situ. This method uses the fact that the angle of the linearly polarised light is shifted due to the birefringence of the atoms in the presence of a magnetic field. As such, the angle of the linearly polarised light after the the atoms has some spatially varying profile which has been rotated by the Faraday angle $\theta_F(x,y)$. The variations in the polarisation angle are measured using a linear polariser before measuring the intensity of the light on a camera where Malus' law $(I_A(x,y) = I_0(x,y)\cos^2(\theta_F(x,y) + \theta_0)$, where θ_0 is the initial angle of the light to the polariser's axis) gives the relationship between polarisation angle and intensity. For low densities, the resulting signal is proportional to the square of the density, so using Faraday

imaging is more sensitive to fluctuations in intensity in that range, but also struggles to image low density clouds. This method also produces sharper images than absorption imaging as it does not require an optical pumping step.

3.3 Previous attempt to observe BEC superfluid fountain effect at UQ

In 2015, Giullaume Gauthier (who was then a PHD student in the lab) and his supervisor Tyler Neely attempted to perform an experiment to look for the superfluid fountain effect in a BEC. Figure 3.2 below depicts the DMD sequence which they ran to obtain their results which can be seen in Fig. 3.3.

The results depicted in Fig 3.3 **a** are suggestive of a fountain effect with the relative fraction thermal components (red and blue circles in Fig 3.3 **a**) not changing significantly over the time scale of the experiment. Additionally, the condensate parts (red and blue squares in Fig 3.3 **a**) appear to start oscillating, although the experiment is not run for long enough to say for sure whether it is oscillations that we are beginning to see. There are a few points which make the results inconclusive. The largest issue was it was suspected that thermal atoms were both in and outside the DMD pattern but still trapped within the red sheet (i.e. the DMD could not contain the thermal atoms) meaning the two reservoirs may have been in thermal contact at an unknown time scale. This is an issue for the experiment because the only thermal coupling, if indeed there is any, between the two reservoirs should be through the channel. They attempted to mitigate this by shining near-resonant light outside the DMD pattern as well in an effort to excite any thermal atoms outside the DMD out of the red sheet, but the results were not satisfactory. One other minor experimental details which make this an inconclusive experiment are that it was not run for long enough to fully see the effect (if indeed it is present).
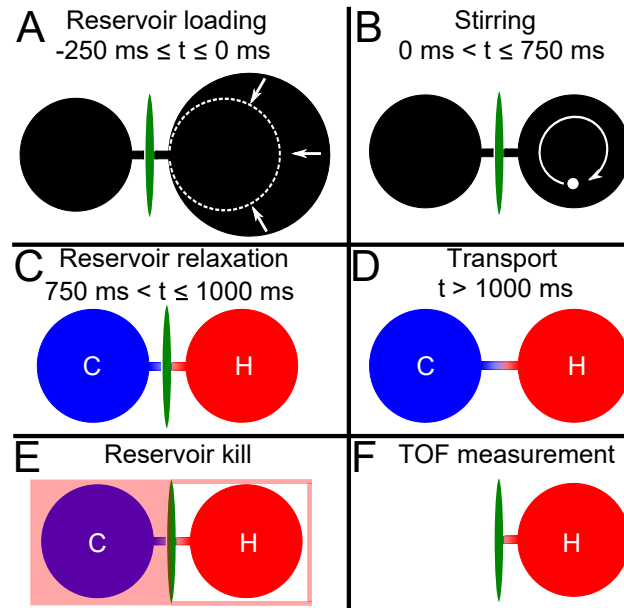
FIGURE 3.2: Credit Guillaume Gauthier. DMD sequence used to perform experiment whose results can be seen in Fig. 3.3. The reservoir to be heated is shrunk down initially so before the heating, it has more atoms than the other as the stirring step excited some atoms out of the trap, but after heating the atom number is the same. To remove atoms, near resonant light was shone on one side of the DMD pattern to excite all the atoms in that reservoir out of the trap so TOF analysis could be performed on just one reservoir.

3.4   New Optical Box Trap

The optical box trap has been implemented this year (2019) to UQ's BEC lab where the design was inspired from the work of Ville et al. [28]. The optical system which creates the 'green sheets' needed for vertical confinement in the box trap is depicted in Fig. 3.4 and Fig. 3.5, which are the bottom and top optical tables respectively. In essence, it splits a blue-detuned 532nm beam into two beams before interfering them at the atoms. Their interference pattern creates a stack of repulsive laser sheets (also known as an 'optical accordion'), between which atoms can be confined vertically creating a very weakly harmonic anti-trapping potential. The result is a very flat trap (i.e. a trap where the intensity of the light does not vary notably across the length scale of the experiment) with a trapping frequency of 58(1) Hz and lifetime of 18(5) seconds (see Fig. 3.6 and 3.7 for these characterisation results).
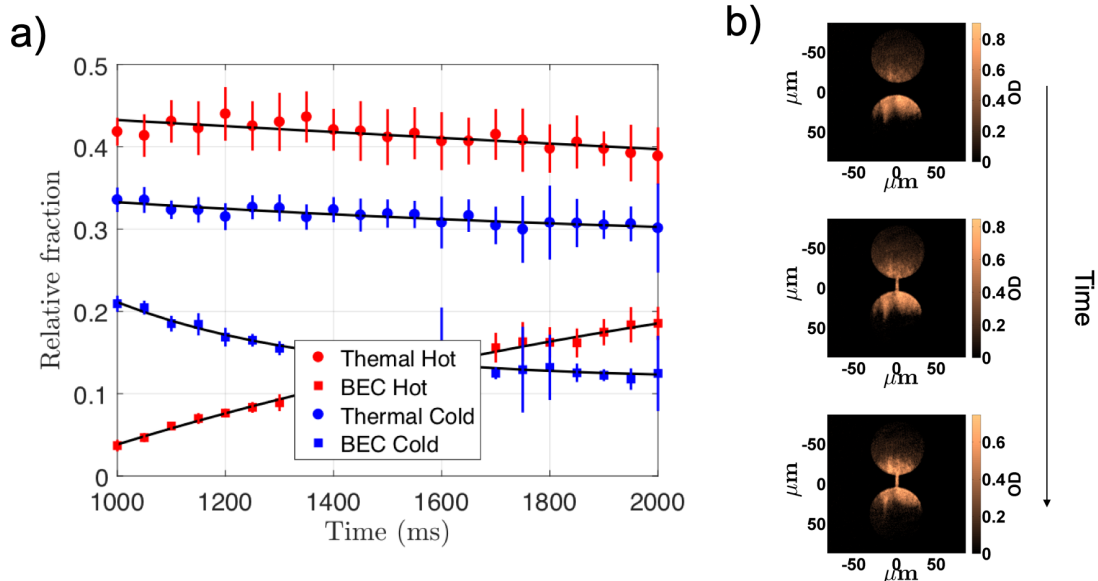
FIGURE 3.3: Adapted from images provided by Guillaume Gauthier. **a)** Results from previous attempt to see SFE in a BEC from TOF measurements. The relative fraction is defined as N_i/N_{tot}, where N_i is the atomic population in one of the categories in the legend and N_{tot} is the total atomic population. In the legend, 'Hot' refers to the reservoir which has been heated and 'Cold' refers to the other, while 'Thermal' and 'BEC' refer to the two components of an experimental BEC. The fits to the data are exponential: $A = A_0 e^{-\alpha t}$ where the time constants α are: Thermal Hot = (9511 ± 105)ms, BEC Hot = (1492 ± 700)ms, Thermal Cold = (1318 ± 300)ms, BEC Cold = (364 ± 110)ms. **b)** Top-down in situ images from previous attempt to see superfluid fountain effect in a BEC. Top image is after heating but before any transport with the middle image being soon after the channel is opened and the final image is at the end of the experimental run.

The optical box trap eliminates the major issue experienced when the fountain effect was looked for previously in the red sheet - namely that now any atoms outside the DMD pattern are expelled from the trap. This is an important feature for isolating either one of the reservoirs for measurements with time-of-flight (TOF), see Section 4.1. Another feature of the green sheet's effectively anti-harmonic nature which could be explored in the future is it could be used in conjunction with the red sheet's harmonic nature to create a completely flat trap.
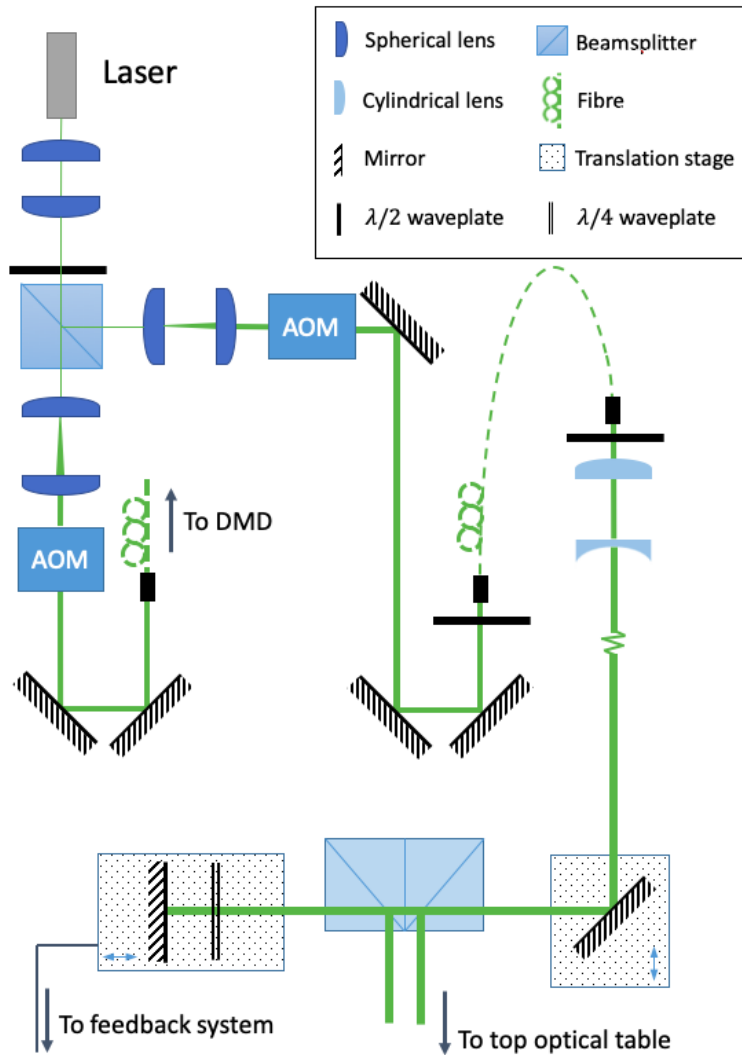
FIGURE 3.4: Credit to Maarten Christenhusz. The optical system for the 532nm light on the bottom table of the experiment. The laser is expanded using two spherical lenses before being split with one path going to the DMD and the other to the green sheet. Following the green sheet path, the beam is then further magnified before the acousto-optic modulator (AOM) diffracts the first order to be coupled into the optical fibre. The fibre couples the bottom table to the top table (Fig 3.5). The cylindrical lenses then elongate the beam in one dimension turning the symmetric Gaussian beam into an elliptical beam. The elliptical beam is then sent through two beam splitters which create the two beams needed to interfere at the atoms in the science cell and create the green sheets needed for the vertical confinement in the optical trap.
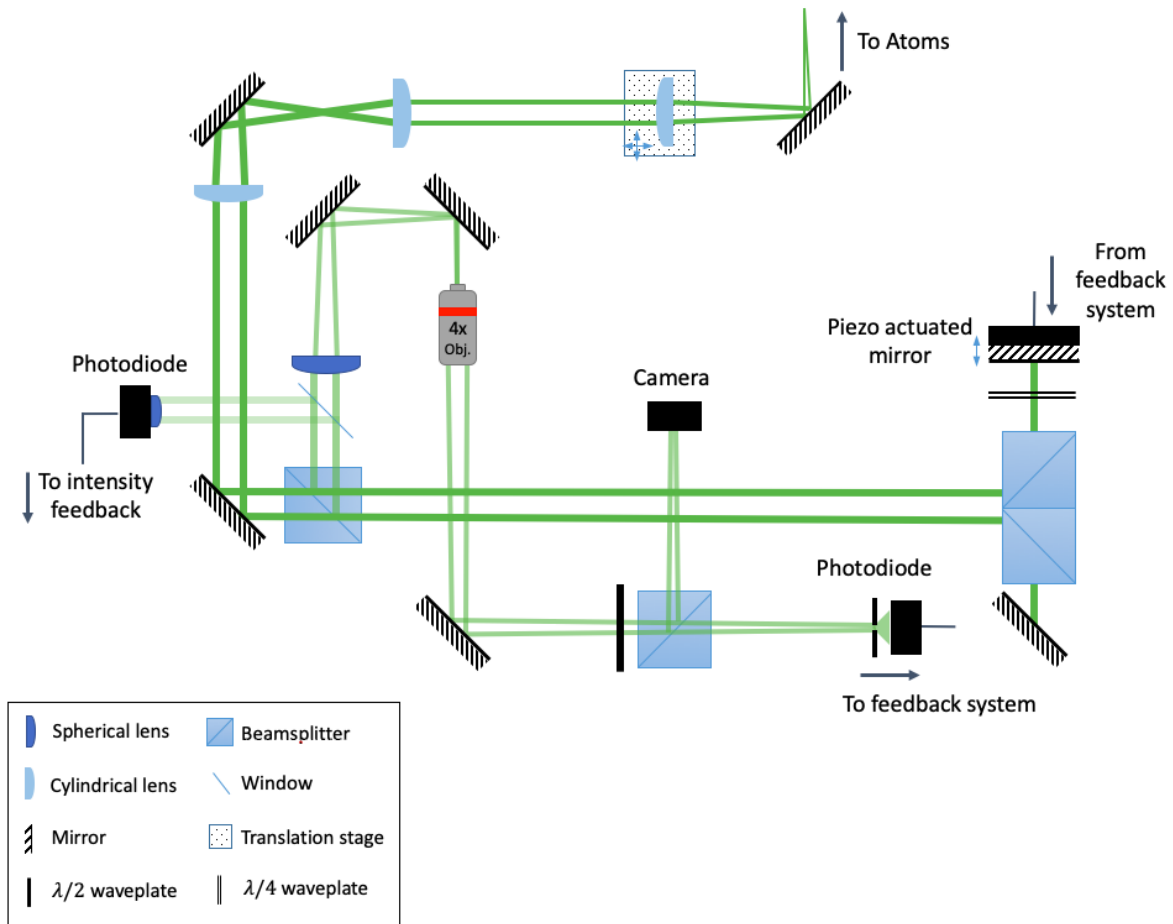
Figure 3.5: Credit to Maarten Christenhusz. Continuing on from the bottom table depicted in Fig. 3.4, this is the optical system for the green sheet on the top table of the experiment. The phase of the beam which reflects off the piezo actuated mirror is controlled by moving the position of that mirror in the non-common path. The first beam splitter after the two beams have been created send some of the light to the active phase stabilisation which ensures the phase of both beams is the same through the control of the piezo actuated mirror. The active phase stabilisation works by using a pin hole (immediately before photodiode), which samples a small section of the interference pattern (ideally the point of maximum intensity) onto a photodiode. Using a P.I. controller connected to the photodiode and the piezo, it moves the piezo in response to any fluctuations in the intensity to ensure the two beams' phases are the same and the final interference pattern remains stable. The effectiveness of this stabilisation can be seen by the lifetime comparisons with and without stabilisation in Fig. 3.7. The camera in the feedback path allows for a visual check of the interference pattern. The second and third final lenses columnate the beams before the final lens focuses the two elliptical beams onto the atom plane and interferes them to create the optical lattice.
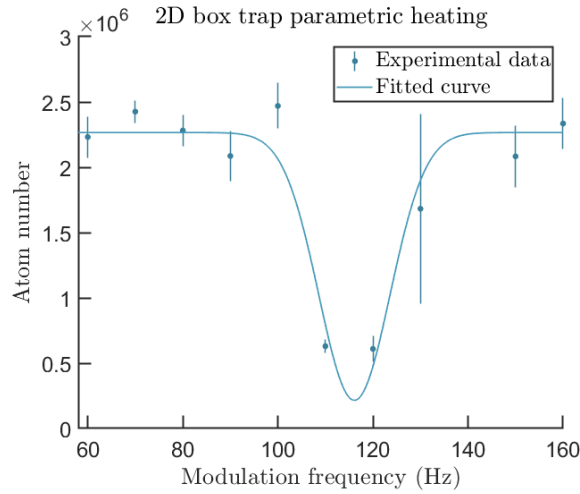
FIGURE 3.6: From data I collected with Maarten Christenhusz. Results from modulating the vertical position of the green sheet to parametrically heat the BEC in the box trap. The decrease in atom number at 116 Hz is due to the modulation being at the resonant frequency of the atoms thus exciting them out of the trap. The trapping frequency is half of this resonance frequency. So the vertical trapping frequency of the box trap is 58(1) Hz. Each data point is an average of 5 measurements with 95% confidence intervals for error bars. The fit is a Gaussian: $y(f) = -A\exp(-(f-B)^2/D^2)+C$, where A, B, C, D are coefficients to be fitted with B giving the resonance frequency and f is the modulation frequency.
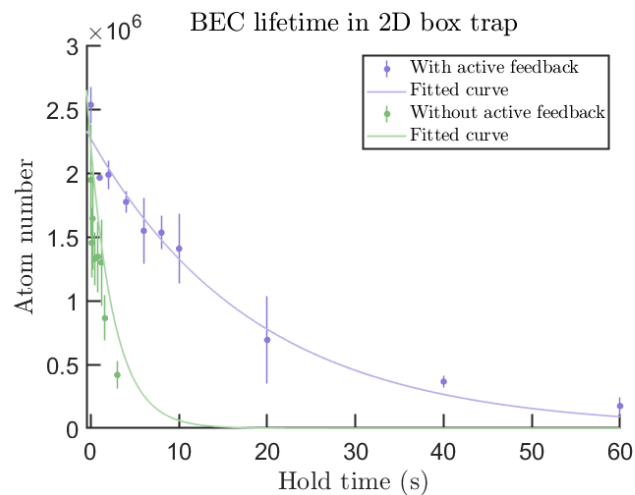
FIGURE 3.7: From data I collected with Maarten Christenhusz. Lifetime results in the box trap with (blue) and without (green) the active feedback stabilisation where the fits plotted are an exponential decay $y(t) = A\exp(-t/B)$, where A and B are coefficients to be fitted with B giving the lifetime and t is the hold time. The lifetimes are 18(5) seconds and 3(2) seconds respectively. Each data point is an average of 3 measurements when the lock was used and 4 measurements without the lock with 95% confidence intervals for every error bar.

While the use of the box trap is needed to perform the experiment without the un-known effect of unwanted thermal contact between the reservoirs, the flatness of the trap and the anti-trapping nature takes the situation beyond the numerical situations approached in Refs. [23, 24]. In those situations, they only predict the fountain effect in a harmonic trap. While the green sheets which are part of the box trap are effectively anti-harmonic, perhaps the its flatness will make the time scale of the experiment long, although this may not be an issue with the relatively long life time of the box trap.

This trap also has the potential to have configurable fringe spacing, and potentially create a true 2D trap for BECs.

4

Progress Towards Looking for the Fountain Effect in a BEC

Before being able to perform the experiment in which we look for the superfluid fountain effect, there are a number of prerequisite tests to be carried out. These will ensure each step of the preparation and transport in the experiment will work and the data can be analysed accurately. Figure 4.1 illustrates the DMD sequence which is planned to be performed in order to look for the superfluid fountain effect.

From Fig. 4.1 one can see there are a number of steps which need to be tested including the heating of the BEC and testing the transport of the condensate and thermal atoms in the dumbbell configuration. As the optical box trap is yet to be used for any transport experiments at UQ, an experiment of condensate flow in the dumbbell is performed and

reported on in Section 4.1. In Section 4.2, I report on the experiments I carried out to test the heating of the BEC in both the red sheet and optical box trap. I considered different methods of heating, rate of heating and determining the temperature of the thermal cloud from time-of-flight (TOF) analysis.

The results presented in the following sections are somewhat incomplete as the experiment was out of action for much of my honours year both while the optical box trap was being implemented and due to a number of breakages of key pieces of equipment, the last of which was a failure in the vacuum system. This is talked about more in the conclusion of the thesis, but it should be noted that this has meant that some issues which arose after the measurements were analysed could not be readdressed. One issue however which was addressed was the inconsistency of the code used to analyse TOF images of low condensate fraction BECs. Section 4.2.1 outlines the improvements made to the fitting code which improved the accuracy and reliability of the data.
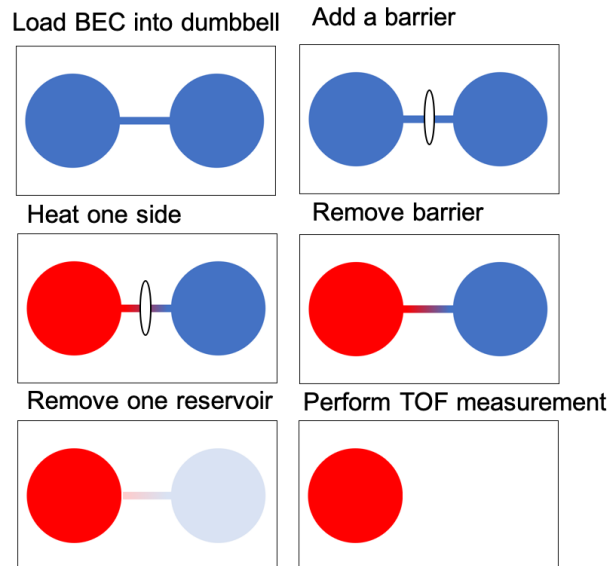

FIGURE 4.1: DMD sequence which is intended to be used when looking for the superfluid fountain effect in a BEC. The blue indicates a high condensate fraction BEC while the red indicates a heated BEC with a lower condensate fraction. The white indicates where the DMD potential is turned on.

4.1 BEC Transport in the Optical Box Trap

In the UQ BEC lab, the inclusion of the green sheet as the method of vertical confinement in the optical box trap brings with it questions around how it will effect the transport of atoms within it. Of particular interest here is the transport within the dumbbell configuration. As such, I performed an experiment similar to that in Ref. [21] with the atoms trapped in the green sheet instead of the red sheet. To perform this experiment, the DMD sequence outlined in Fig. 4.2 was used.
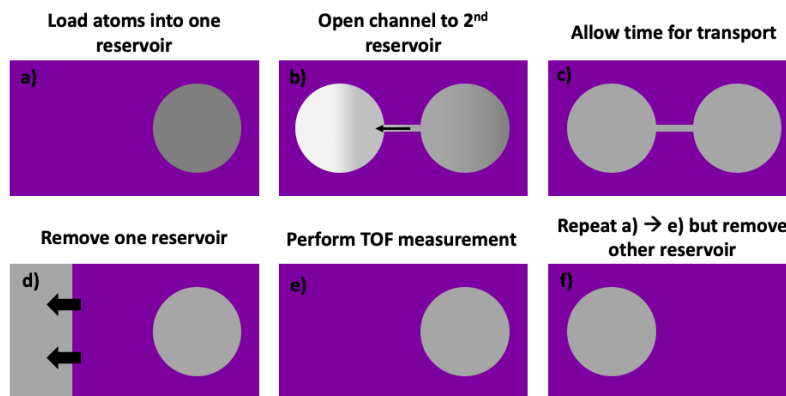
FIGURE 4.2: DMD sequence which was performed to take transport data in the optical box trap. Data corresponding to this sequence is in Fig. 4.4. Here, the grey indicates the BEC with the purple indicating the DMD potential. Step **d)**, which is the method of removing atoms from one reservoir, is elaborated on in the text below and in Fig 4.3.

In order to analyse the data, absorption imaging is used on atoms dropped from the trap giving a TOF image. In order however to obtain data from either reservoir individually, the atoms from the other reservoir need to be removed. The green sheet's anti-trapping nature is helpful for this. By simply turning off one side of the trap [Fig. 4.2 (d)], the atoms are repelled allowing for the clear identification of atoms from just one reservoir which can be counted. A demonstration of the removal of the atoms is illustrated in Fig. 4.3.

Using the method depicted in Fig. 4.2 to run an experiment, the relative atom population in each reservoir is shown in Fig. 4.4 with the in situ images in Fig. 4.5. One can see that the relative population quickly moves towards 0.5 before oscillating about that value. This
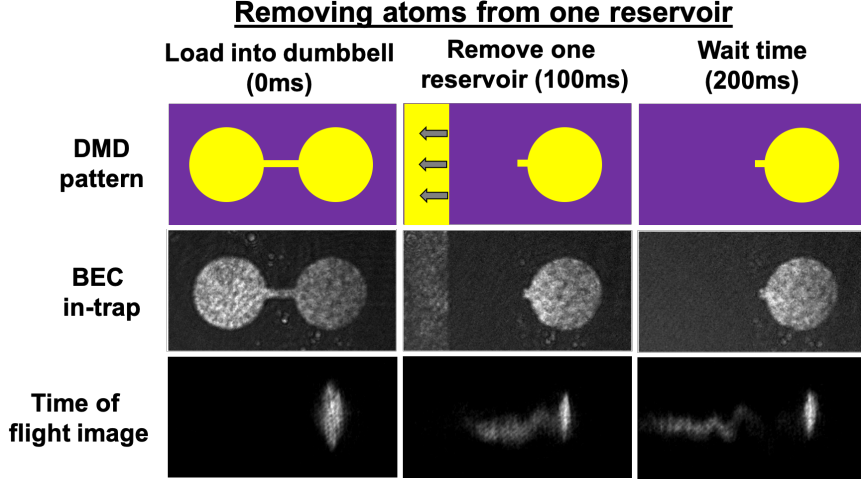
FIGURE 4.3: DMD sequence to remove atoms from one reservoir so TOF measurements can be taken on the other. Once the DMD for one reservoir is switched off, the DMD potential then sweeps from the remaining reservoir across the DMD (see top of central column) to reduce the likelihood of any unwanted atoms escaping into the remaining reservoir. The top row is the DMD potential where purple indicates the DMD potential is 'on' and yellow indicates it is 'off'. The second row is a Faraday image of the BEC in situ at the corresponding stages of the sequence. The bottom row is corresponding TOF absorption images and one can see the atoms being expelled from the trap.

response is similar to the condensate transport simulated in Ref. [23] and seen experimentally in red sheet traps from Refs. [20, 21].

To calculate each data point in Fig 4.4, the populations of the three trials for each reservoir was averaged and then the relative population (η) was calculated from those averages. For example, to calculate the relative population of the left reservoir:

$$\eta = N_L/(N_L + N_R), \tag{4.1}$$

where N_L (N_R) is the number of atoms in the left (right) reservoir. The uncertainties of the relative population means are standard errors (SE):

$$SE = \frac{1}{\sqrt{n}}\sqrt{\frac{\sum_{i=1}^{n}(N_i - N_{\text{avg}})^2}{n-1}}, \tag{4.2}$$

where $n = 3$ is the number of trials and N_i is the atomic population of the reservoir of interest's i^{th} trial. The uncertainties for the relative populations ($\Delta\eta$) are then calculated

like so, using the left reservoir as an example again:

$$\Delta\eta_L = \eta_L \sqrt{\left(\frac{SE(N_L)}{N_L}\right)^2 + \left(\frac{SE(N_L + N_R)}{N_L + N_R}\right)^2}. \tag{4.3}$$
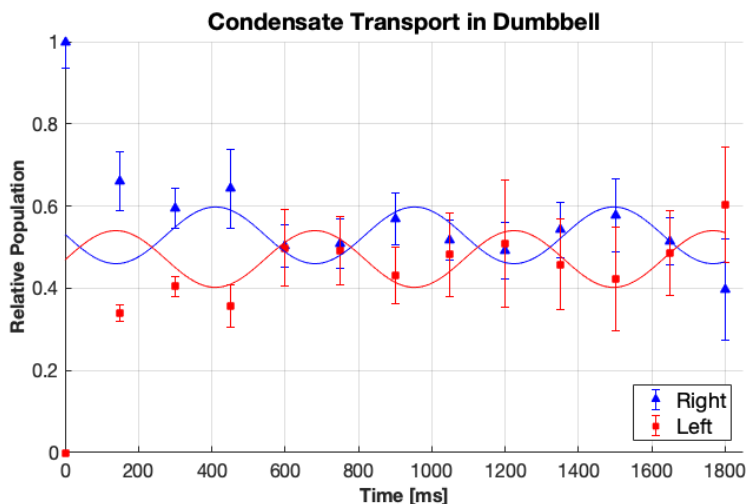
Figure 4.4: Results from TOF images of condensate transport in dumbbell and optical box trap where the left reservoir is initially empty and the atoms are loaded into the right one as seen in Fig. 4.5. Each measurement was made three times to reduce the error. Each errorbar is the standard error from the three measurements. Applying a sine fit to the data points from after time = 400ms onwards gives an oscillation frequency of 1.8(3) Hz for both reservoirs where the uncertainty is a 95% confidence interval.
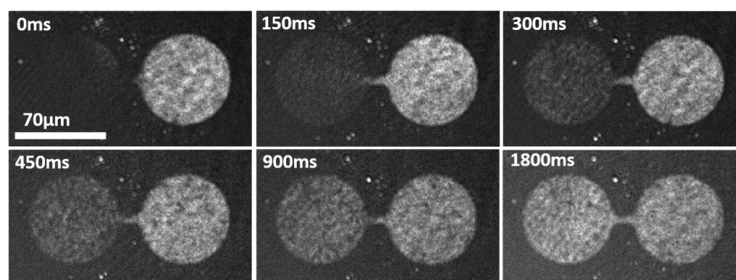
Figure 4.5: Filtered Faraday images of the transport occurring in the dumbbells in situ.

The sine fits applied to the data in Fig 4.4 from times of after 400ms onwards allow for the oscillation frequency of the condensate to be calculated. The fit is only applied after 400ms as this is when the experiment clearly enters the oscillating regime after the initial equilibration of atomic populations. We can compare these results to the acoustic model

developed by Gauthier et al. [21] by inputting the experimental parameters I used in my transport experiment.

The experimental parameters corresponding to the data depicted in Fig. 4.4 and relevant equations are:

$$N = (1.15 \pm 0.05) \times 10^6, \ \omega_z = 2\pi \times 58(3) \text{ Hz}, \ r = 35 \ \mu\text{m}, \ l = 12 \ \mu\text{m}, \ w = 10 \ \mu\text{m}, \quad (4.4)$$

$$m = 86.9 \times u = 1.44 \times 10^{-25} \text{ kg}, \quad (4.5)$$

$$a = 99a_0, \quad (4.6)$$

$$A = 2\pi r^2 + lw = 7.82 \times 10^{-9} \text{ m}^2, \quad (4.7)$$

$$g = \frac{4\pi\hbar^2 a_s}{m}, \quad (4.8)$$

$$\mu = \frac{1}{2}\left[\frac{3Ng(m\omega_z^2)^{1/2}}{2A}\right]^{2/3} = 1.44 \times 10^{-31} \text{ J/kg}, \quad (4.9)$$

$$c = \sqrt{\frac{\mu}{m}} = 1.00 \times 10^{-3} \text{ m/s}, \quad (4.10)$$

$$l_z = \sqrt{\frac{2\mu}{m\omega_z^2}} = 3.88 \times 10^{-6}\text{m}, \quad (4.11)$$

$$V = 2\pi r^2 l_z = 2.99 \times 10^{-14} \text{ m}^3, \quad (4.12)$$

$$S = 2wl_z = 7.76 \times 10^{-11} \text{ m}^2, \quad (4.13)$$

$$\delta = 2.14\sqrt{S} = 1.89 \times 10^{-5} \text{ m}, \quad (4.14)$$

$$\omega = c\left[\frac{S}{l+\delta}\left(\frac{1}{V_1} + \frac{1}{V_2}\right)\right]^{1/2} = 2\pi \times 12.98 \text{ Hz}, \quad (4.15)$$

$$f = \frac{\omega}{2\pi} = 2.07(6) \text{ Hz}, \quad (4.16)$$

where N is the total number of atoms in the system (I've taken it to be the average number of atoms from all the measurements after 400ms as the atom number was decreasing over the experiment with the uncertainty being the standard error), ω is the vertical trapping frequency of the green sheet, r is the radius of one reservoir, l is the length of the channel, w is the width of the channel, m is the mass of the rubidium 87 atoms, a is the s-wave scattering length, $V_1 = V_2 = V$ is the volume of one reservoir, l_z is the Thomas-Fermi radius in the z-direction, A is the total area of the potential, g is the pre-factor from the GPE, S is

the cross-sectional area of the channel, δ is the end correction, ω is the angular frequency of the oscillations, c is the speed of sound in the condensate, μ is the chemical potential and f is the frequency of the oscillations. The final oscillation frequency uncertainty is from carrying through the uncertainties in N and ω_z (see Appendix for matlab code which calculated the uncertainties).

Comparing this frequency from the model [2.07(6) Hz] to the frequency from the data [1.8(3) Hz], the acoustic model from Ref. [21] agrees with my experimental transport data within the uncertainties. One approximation which is made in this model is the chemical potential is a 2D approximation, whereas the BEC in my experiment is a 3D BEC. The paper found that this approximation leads to the speed of sound (c) to be about 5% larger than the 3D case. Applying this correction would bring the theoretical oscillation frequency closer to my measured value. This results is a demonstration of the applicability of the acoustic model to a dumbbell in an box trap, that the condensate transport is qualitatively (superfluid relative population equilibrating then oscillating about 0.5) and quantitatively behaving as we expect and it demonstrates that the data collection method is appropriate. Unfortunately, the vacuum system failure meant that superfluid flow in more channel sizes could not be tested. The large uncertainties in each data point was due to the active phase stabilisations inconsistency throughout the entirety of the data acquisition time period (it became unlocked at one stage mid-experiment and needed to be re-locked).

4.2   Heating a BEC

The heating of a BEC is generally an unwanted side effect in BEC experiments and can come about due to time-varying imperfections in the optical trap and off-resonant scattering of photons. However, in my experiment, the controlled heating of the BEC in one reservoir is required to create the temperature difference which drives the superfluid fountain effect. To heat a BEC, one can, as you would with a classical fluid, perform work on it. I considered a few different methods of heating using the DMD to force the BEC to move around and

excite some particles out of the lowest energy state and into the thermal cloud. Figure 4.6 depicts the considered heating methods including 'bubbling' and 'shaking'. The bubbling method was suggested by Kwan Goddard-Lee (an honours student in the lab at the time) while the shaking method of heating was inspired by Navon et al. [29]. The bubbling and shaking methods are alternate methods to what has already been used to heat BECs at UQ. The previous methods of 'stirring' (previously used to heat a BEC) and 'pumping' (inspired by Ref. [26] where they used it to test the DMD's time averaging effectiveness but also found it to heat the BEC), which can also be seen in Fig. 4.6 were found to kick many atoms out of the trap thus reducing the overall atom number. This results in an extra DMD step to create an initial imbalance in population in the two reservoirs in anticipation for atom loss due to heating. Bubbling and shaking were considered as alternatives to see if they could heat the BEC and to see if they could do so without exciting atoms out of the DMD trap.
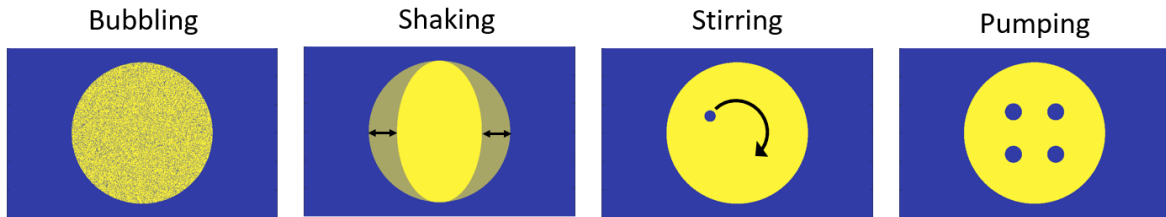
FIGURE 4.6: DMD patterns which could be used to heat a BEC. Bubbling turns on a random selection of a given fraction of the mirrors and changes them at a given frequency. The image above has 20% of the mirrors turned on in the circle (i.e. a 'fill factor' of 0.8). Shaking moves the edges of a circle (in one dimension) back at forth to heat the BEC. Stirring moves a barrier around in circles within the reservoir. Pumping turns on and off entire sections of the reservoir.

4.2.1 TOF analysis to determine condensate fraction and thermal cloud temperature

The condensate fraction is a measure of how much of the BEC has been heated and it can be determined through a bimodal fitting technique from the TOF images. By turning off all the traps holding onto the BEC, it falls under gravity allowing for it to expand freely. The experimentally created BECs have two parts, the condensate and the thermal cloud, both of which expand differently under free evolution expansion. The thermal cloud has a Boltzmann momentum distribution, so it expands like a Gaussian in the limit of long free

expansion evolution. Thus, the following Gaussian fit can be applied to a TOF absorption image to determine the cloud's waist and the number of atoms in the cloud,

$$n_T(x, z, t) = A_T(t)e^{-\left[\frac{x-x_0^T(t)}{\sigma_x^T(t)}\right]^2 - \left[\frac{z-z_0^T(t)}{\sigma_z^T(t)}\right]^2}, \tag{4.17}$$

where $A_T(t), x_0^T(t), \sigma_x^T(t), z_0^T(t), \sigma_z^T(t)$ are free parameters to be fitted to the integrated thermal density profile $n_T(x, z, t)$ [27]. Note that x is the direction perpendicular to the direction of gravity (i.e. horizontal) while z is parallel to gravity (i.e. vertical). The characteristic length scales of the expanding cloud evolve as,

$$\sigma^2(t) = \sigma^2(0) + \sigma_0^2 t^2, \tag{4.18}$$

where $\sigma_0 = \sqrt{2k_B T/m}$ [30]. As well as knowing how much of the BEC has been heated, I am interested in how vigorously it has been heated and determining the temperature of the thermal cloud could provide insight into this. By plotting $\sigma_x^2(t)$ or $\sigma_z^2(t)$ against t^2, you expect a linear relationship, the slope of which is σ_0. Rearranging σ_0 thus allows for the determination of the thermal cloud's temperature,

$$T = \frac{s \times m_{Rb}}{2k_B}, \tag{4.19}$$

where T is the temperature of the thermal cloud, s is the slope of a linear fit to a TOF^2 vs (thermal waist)^2 plot and m_{Rb} is the mass of a rubidium atom.

The condensate part of an experimentally realised BEC expands differently to the thermal cloud because of their different momentum distributions. As such, the following integrated column density can be fit to the cloud assuming a Thomas-Fermi approximation,

$$n_C(x, z, t) = A_C(t)\left[1 - \left(\frac{x - x_0^C(t)}{\sigma_x^C(t)}\right)^2 - \left(\frac{z - z_0^C(t)}{\sigma_z^C(t)}\right)^2\right]^{3/2}, \tag{4.20}$$

where $A_C(t), x_0^C(t), \sigma_x^C(t), z_0^C(t), \sigma_z^C(t)$ are free parameters to be fitted to the integrated thermal density profile $n_C(x, z, t)$. The entire cloud can then be fitted with a bimodal fit where n_T and n_C are summed: $n(x, z, t) = n_T(x, z, t) + n_C(x, z, t) + n_0$, where n_0 is some constant

offset.

Prior to this thesis, the fitting mechanism simply applied the bimodal fit using Matlab's nonlinear least square method once assuming that the center of the thermal cloud and condensate were the same position. For BECs where this assumption is true and when condensate fractions are greater than about 0.1, the fits are fairly accurate as can be seen visually and the low root mean square error (RMSE) values (as low as 0.032) on the fits to the TOF data.

In the work I am interested in however, where I am heating BECs to low condensate fractions, the fit can fail. As such, I have made some adjustments to the fitting code to increase its reliability in these cases.

The primary adjustment I've made is I've removed the constraint that the centres of the thermal cloud and condensate are the same (i.e. $z_0^C(t)$ and $x_0^C(t)$ do not necessarily equal $z_0^T(t)$ and $x_0^T(t)$ respectively). This is the primary alteration with the further changes outlined below used to coax the fit to work as well as possible for low condensate fractions.

I then found that for small condensate fractions, the code would fit a condensate with a width larger than the thermal cloud's width in the x direction (i.e. $\sigma_x^C > \sigma_x^T$) even when this is clearly incorrect (see Fig 4.7 for example). Note that in the x direction the thermal cloud expands faster than the condensate, so having a condensate width larger than the thermal cloud width is indicative of the fit failing. If this is the case, the starting points for A_C and A_T would be selected to be the same and the maximum OD value from the data. Additionally, the starting points for the condensate widths would be the thermal cloud widths from the previous fit and visa versa. One other check which is made in the code is if the maximum value of n_C is larger than n_T. If it is not, the starting values for A_C and A_T are switched.

This updated and improved fitting method is used for all the data analysis in this thesis

For high condensate fraction BECs, the condensate expansion in the z direction maybe faster than the thermal cloud's. So, unlike in the x direction, the thermal width may be legitimately smaller than the condensate width in the z directions. If this is the case, the code struggles to accurately fit that cloud. Unfortunately, I was not able to modify the code to improve this fitting resulting in less accurate condensate fractions and thermal widths of fittings when this is the case.
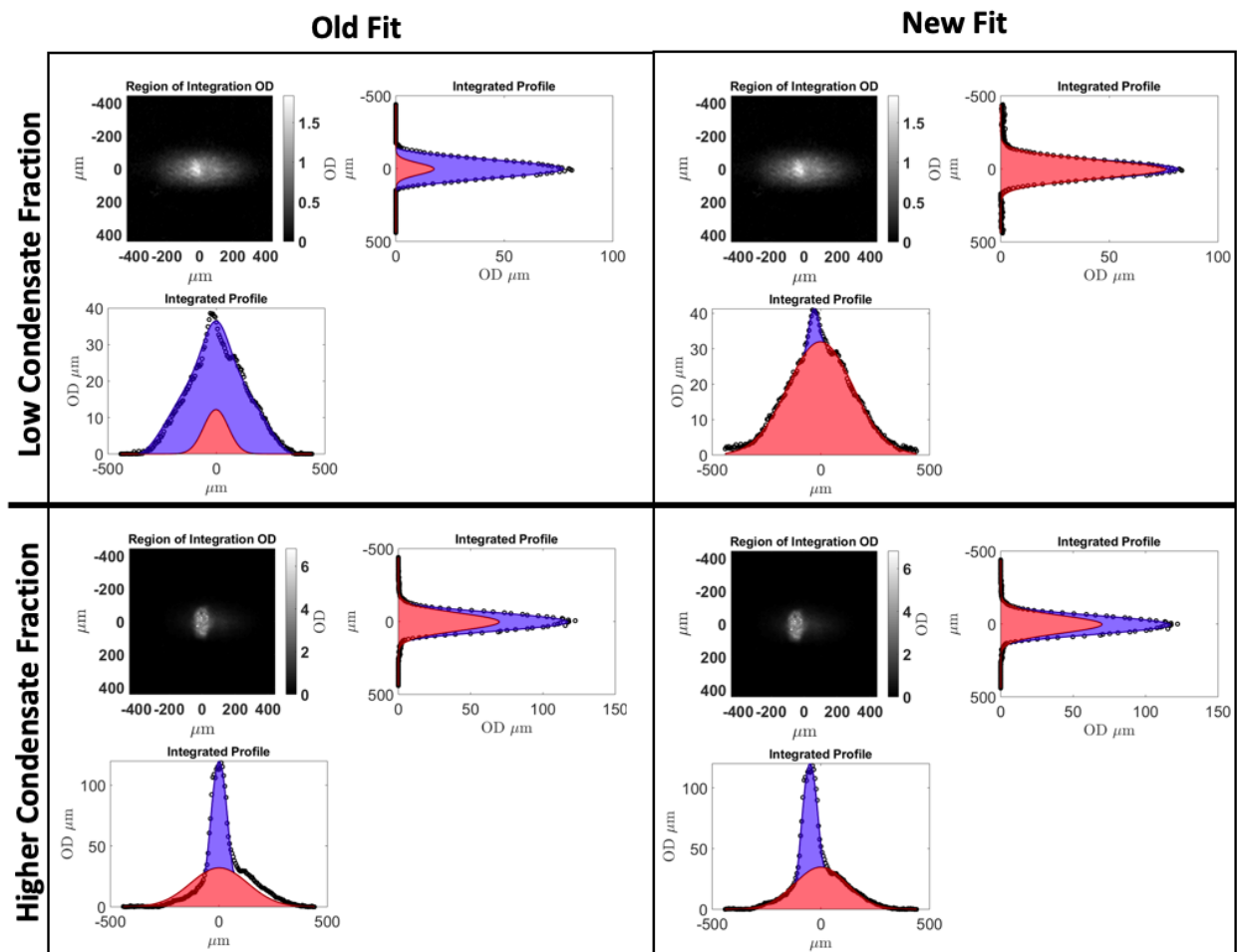
FIGURE 4.7: Two situations where the new fitting (right column) improves on the old fitting (left column). The top row is a low condensate fraction (about 0.04) situation where the old fit is clearly incorrect and the new fit on the right is much better. The bottom row is a higher condensate fraction (about 0.38) situation where the condensate and thermal cloud don't share the same center and the new fit deals with it better qualitatively and improves the RMSE from 0.161 to 0.133.

4.2.2   Results and analysis

Here I report on the data from two heating experiments. The first is in the red sheet (data taken before optical box trap was implemented) where shaking was used to see how the frequency effects the temperature and condensate fraction, as well as to see how the atom number is affected by the heating. I was also interested to see if there is a frequency at which the shaking creates a time-averaged trap and no longer heats the BEC. The second experiment is in the optical box trap where a simple test was performed to try and accurately determine the temperature of the trap using the bubbling technique.

Results from heating in the red sheet

These results demonstrate a few important things for looking for the superfluid fountain effect in a BEC. Firstly, from the condensate fraction plot in Fig. 4.8, we can see that the BEC can be heated gradually by increasing the frequency of the heating method up until the condensate has been heated totally into a thermal cloud. This sort of a plot is important because having good characterisation of how the frequency heats the BEC means that when heating during the fountain effect sequence, we can be sure of what the temperature and condensate fraction will be for a given frequency. This gives us the ability to choose a desired condensate fraction and know what shaking frequency to use. The results in Fig. 4.8 would not however be useful in the superfluid fountain experiment because this was performed in the red sheet whereas the final experiment would be performed in the optical box trap.

Regarding the temperature, it reaches a maximum value quickly and plateaus before the cloud is entirely thermal. This is because the red sheet trap was not deep enough to hold atoms with higher temperatures as they have enough kinetic energy to escape. This leads to the decrease in the atom number after 60 Hz (bottom plot in Fig. 4.8).
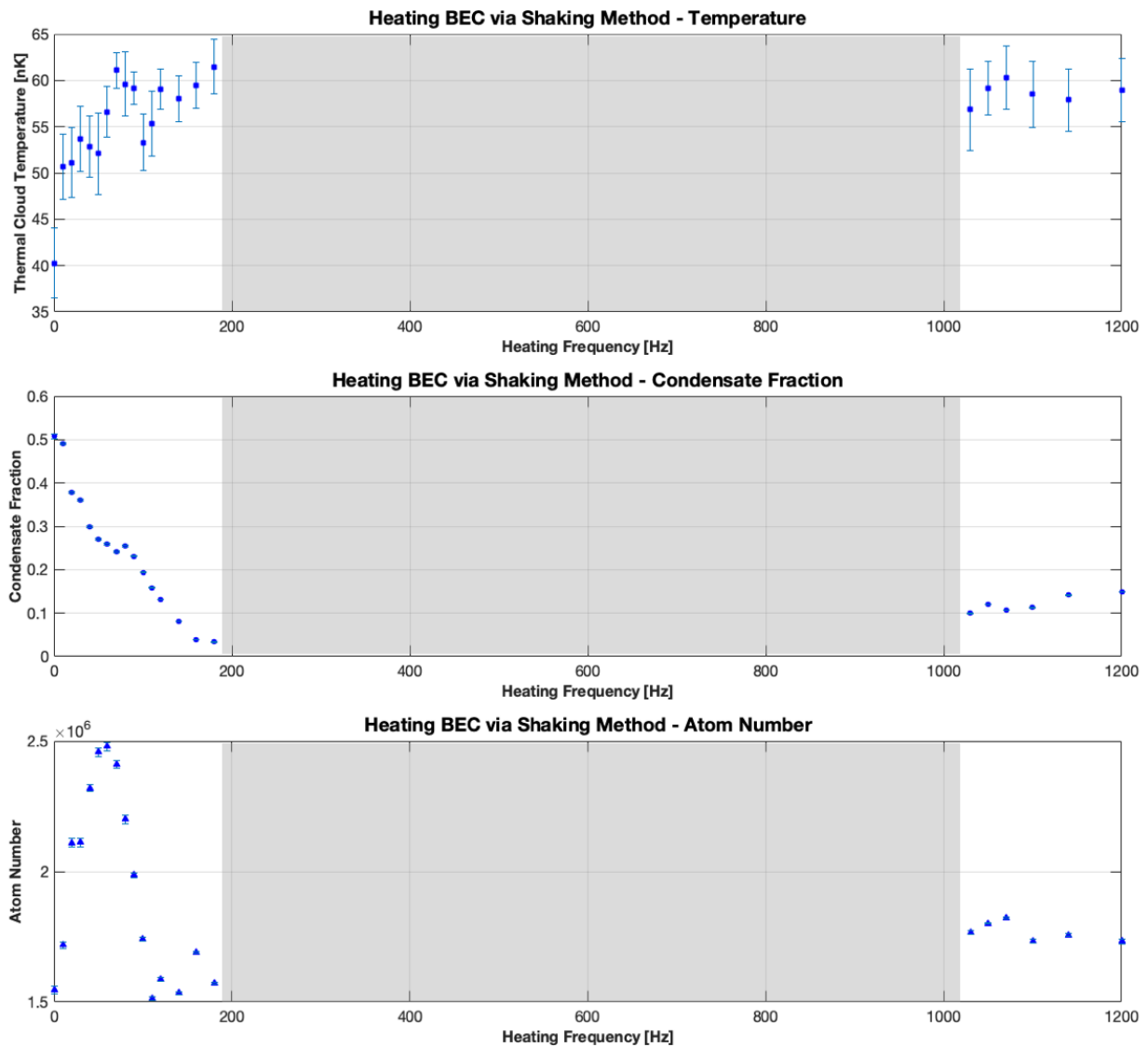
Figure 4.8: Results of temperature, condensate fraction and atom number from heating a BEC in a 100 μm diameter disc using the shaking method over a range of frequencies for 2.5 seconds. The change in the radius of the circle in the dimension of the shaking was 6 μm for each 'shake'. Each temperature data point is calculated from three trials of measurements made at TOFs of 20, 25 and 30 ms using just the vertical expansion. The horizontal thermal cloud expansion did not expand but instead seemed to oscillate in width with an amplitude of a few μm as the cloud fell. The thermal cloud had already expanded in the red sheet out of the DMD before the traps were turned off. Additionally, in free-fall, there appeared to be some barrier restricting any further expansion. As such, all temperature values were calculated using the vertical thermal cloud widths. The condensate fraction and atom number measurements are averages of the 9 measurements taken at each frequency. All uncertainties are the standard error. The shaded region indicates frequencies at which the BEC had been heated totally into a thermal cloud. As such, fewer than 3 measurements were taken at each point in this frequency range to simply check that there was no condensate. These measurements in the greyed range are not displayed in the plots because, once the condensate was destroyed, the effect of interest was to see if there would be a time averaging effect, which the high frequency measurements are indicative of.

The atom number initially is low, and it builds up to a maximum at 60 Hz before decreasing again. The atom number at frequencies below 60 Hz is incorrect and lower than the number actually present. The inaccuracy is due to the camera being saturated for high condensate fractions where the atomic density is very high in the condensate. As a result, the condensate number is under-counted leading to a total atom number also being under-counted. From the data after 60 Hz, the camera is no longer saturated and the condensate number is counted more accurately leading to a more accurate total number.

As we are interested in the atom loss caused by heating, the decrease in atom number after the apex is undesired. Thus, it is clear that shaking is a method which causes many atoms to escape the red sheet trap at this trap depth. We cannot say whether atoms are also lost due to heating before 60 Hz, but one would expect that trend continues. This under-counting also means that the condensate fractions are unreliable before 60 Hz heating. Indeed after 60 Hz, the decay appears to be exponential, and considering the condensate fractions before 60 Hz are all expected to be higher, the decay may be exponential.

There are methods which can be used to reduce the saturation on the camera. One method I considered was detuning the imaging light further from atomic resonance. This however leads to under-counting the thermal atoms. As this data set was taken in part to measure the temperature and to see when the condensate fraction disappeared and reappeared due to the heating and time averaging, accurate measurements of the thermal cloud was more important than that of the condensate in this instance.

The data in Fig. 4.8 was analysed using the updated fitting method. Comparisons between the goodness of fit for the original and updated analysis code for each data point in Fig. 4.8 can be seen in Fig. 4.9. The statistics of the improvement are displayed in Table 4.1. It's clear that the new code always improves the goodness of fit, even for data that the original code fits the data well. Table 4.1 compares the RMSE values for the original and update fitting code illustrating that, on average that there is nearly a 20% RMSE improvement. The RMSE for the new code can still be relatively high (see Fig. 4.10), but these high

values are for measurements where the camera was saturated and the condensate number was under-counted. The RMSE decreases rapidly in both the original and updated fitting code once the condensate fraction is accurately counted (see Fig. 4.10).

On can see from Fig. 4.9, before the trap is time averaged, that the updated fitting improves the fit more as the condensate fraction decreases up until very low condensate fractions, at which point the old fits are very unreliable. This highlights that the RMSE values can't tell if the fit is fitting the data correctly. Fig. 4.7 gives an example where the fit is clearly incorrect for a low condensate fraction, but the RMSE value doesn't reflect the significant improvement the updated code provides (old RMSE = 0.062, new RMSE = 0.050).
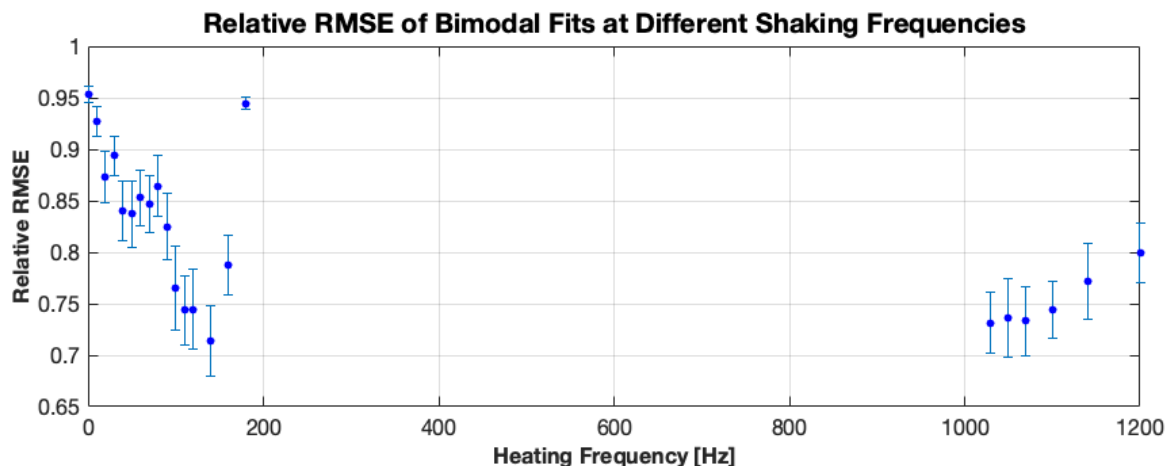
FIGURE 4.9: Relative RMSE ($\mathrm{RMSE_{New}}/\mathrm{RMSE_{Old}}$) for red sheet heating data.

Fit Version	Median	Mean	Standard Deviation
Old Fit	0.090	0.109	0.051
New Fit	0.073	0.092	0.053
Relative RMSE	0.827	0.815	0.111

TABLE 4.1: Impact of updating fitting code on red sheet heating data. All the values in the 'Old Fit' and 'New Fit' rows are RMSE values while the bottom row data is, for every data point, the RMSE of that fit using the new code divided by the old code.

Figure 4.10: Averaged RMSE values for red sheet heating data using both the old and new fitting codes.

Results from heating in the optical box trap
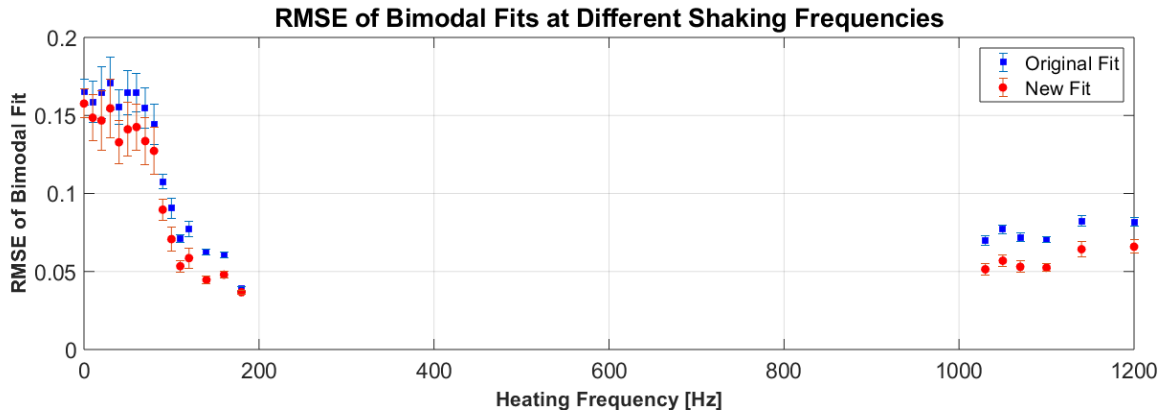
I was able to demonstrate that shaking and bubbling are possible methods to heat a BEC in the red sheet, and I found they were also plausible in the green sheet. After some preliminary tests, I found that shaking removed atoms from the trap more readily than bubbling, so the data below used bubbling. Also, the heating time was decreased from the 2.5 seconds used in the red sheet to 0.5 seconds of heating here to see if heating could be achieved with a shorter time. Again preliminary results suggested this time scale was plausible to both partially and completely heat the BEC into a thermal cloud.

The advantage of the green sheet is that any atoms outside the DMD are repelled, so in the TOF measurements, all atoms being imaged were inside the DMD pattern. This is in contrast to when the red sheet was used and the thermal cloud had already expanded as much as it could before the cloud was dropped. As such, in the optical box trap, the temperature of the thermal cloud could be measured using both horizontal and vertical expansion, and one would expect them to give the same result. This gives us a way of testing the accuracy of our fitting, assuming that the thermal cloud does in fact expand at the same rate in both directions. Testing this is the primary purpose of the results in Fig. 4.11.

While the calculated temperatures from vertical and horizontal thermal cloud expansion
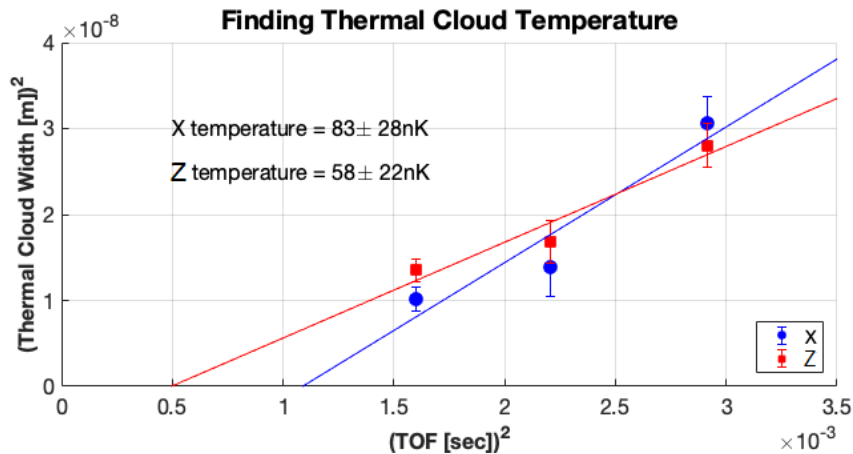
FIGURE 4.11: Optical box trap - after heating using bubbling at 800Hz and 0.9 fill factor in a 70 μm diameter disc. Time of flight values are 40, 47, 54 ms. Three trials were averaged and the errorbars are the standard error. The fits are linear with their slopes being used to determine the temperature of the thermal cloud.

overlap when considering the uncertainties, the relative errors for each temperature is significant (X: 0.34, Z: 0.38) and the data does not look obviously linear. For this data, the thermal width in the z direction was less than the condensate's leading to the aforementioned inaccuracies in thermal cloud fitting. The uncertainties here and the two temperatures not being more similar illustrate the importance of needing to improve fitting this type of result to get more accurate and reliable results.

One expected advantage of the green sheet was that it was expected to be able to confine thermal atoms inside the DMD trap (unlike the red sheet). Unfortunately, at the time of taking the measurements, the trap could not hold on to thermal atoms for very long. Preliminary tests showed that after heating the BEC to a condensate fraction of about 0.3, which was measured after dropping the atoms immediately after heating, when the atoms were held for 500 ms before being dropped, almost all the thermal atoms had escaped the trap. To work out which trap was not deep enough, I increased and decreased the DMD power but that did not effect the rate of thermal atoms leaving the DMD trap. However, changing the green sheet power did. Thus, being able to hold onto more thermal atoms requires more power in the green sheet. This is an engineering problem to be addressed when the experiment is fixed.

5

Conclusion and Outlook

In this thesis, I was able to explore the questions of 'What would the superfluid fountain effect look like in a BEC?' and 'How would we do that experimentally?'. By considering basic superfluid dynamics theory, relevant literature on BEC transport, numerical models and a previous attempt at this experiment, myself and others in the lab developed an experimental method to look for the superfluid fountain effect. In the experimental apparatus, the addition of an optical box trap in 2019 was a key inclusion which allowed me to build on the work done at UQ previously in this search.

In order to test the planned experimental sequence, a number of smaller intermediate experiments were planned and carried out. One of them was the superfluid transport in the newly implemented optical box trap. This experiment is very similar to one performed

previously on the same set up, but in a red sheet [21]. It both qualitatively and quantitatively performed as expected based on all the relevant literature I cited throughout, with the relative population of each reservoir initially equilibrating quickly before oscillating around an equilibrium value. The frequency of the oscillations were then compared to a theoretical value calculated using a model developed in Ref. [21]. The results matched within the uncertainties with the acoustic model giving an oscillation frequency of 2.07(6) Hz and the experimental oscillations were 1.8(3) Hz.

The other intermediate experiment was to test the heating and temperature measurement of the BEC. Qualitatively, the results were positive with the heating methods of bubbling and shaking both demonstrated as possible heating methods which can partially or totally heat a BEC into thermal atoms. Unfortunately though, both methods still removed atoms from the trap. Regarding the measurements to obtain more quantitative data, the condensate fraction, with the improvement I made in the fitting code, appears to be a reliable way to determining the amount of heating which has been done, particularly for low condensate fractions. The fit however struggled to make accurate thermal cloud width measurements in some instances in the green sheet resulting in inaccurate temperature calculations.

This conclusion comes somewhat abruptly in my search or the superfluid fountain effect in a BEC due to the equally abrupt failure of the vacuum system of the apparatus towards the end of my honours year. On the high vacuum side of the experiment (2DMOT), the seal on the 'push beam' window has been compromised due to the Rubidium eating through glass-to-metal seal (Fig. 5.1). Consequentially, the window needs to be replaced and the vacuum achieved again. Beyond not being able to continue the experiment to look for the superfluid fountain effect, the failure in the vacuum also meant that any data that was not taken correctly or displayed unexpected characteristics could not be revisited experimentally.

In order to achieve the vacuum levels required, the magnetic coils which create the magnetic fields used to trap the BEC also need to be removed. These coils have failed multiple times before (including in early 2019) which have resulted in stints of the experiment being unusable. The removal of these coils to fix the vacuum provides an optimal time to redesign
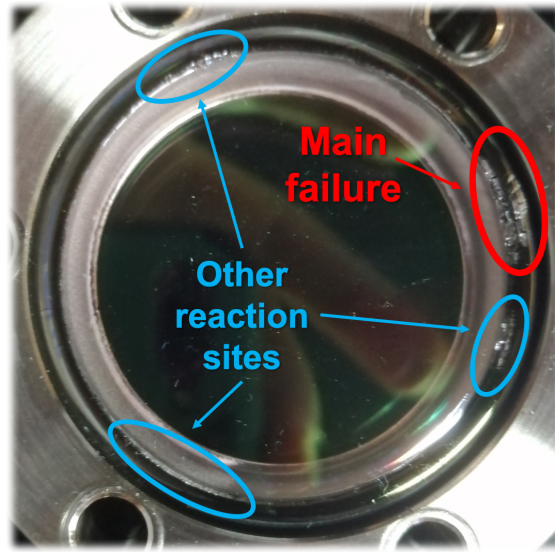
FIGURE 5.1: Image of damage to 'push beam' window due to the Rubidium eating through glass-to-metal seal resulting in the experiment being unable to create a BEC.

and replace their set up to mitigate the issues which have caused the failures. The primary causes have been corrosion of the copper wires (which make the coils), as they are submerged in water for cooling, and heat damage to the insulation between turns of the copper wire from the large currents required to produce the magnetic fields.

Since the beginning of 2019, after the coil failure, I have designed an addition to the coil set up, inspired by Ref. [31], to reduce the load on the BEC coils that dissipate the most power. This addition, called the 'shuttle' (Fig. 5.2), was designed to be compatible with the current coil design (Fig. 5.3), and a redesign which is being work on by Gillaume Gauthier.
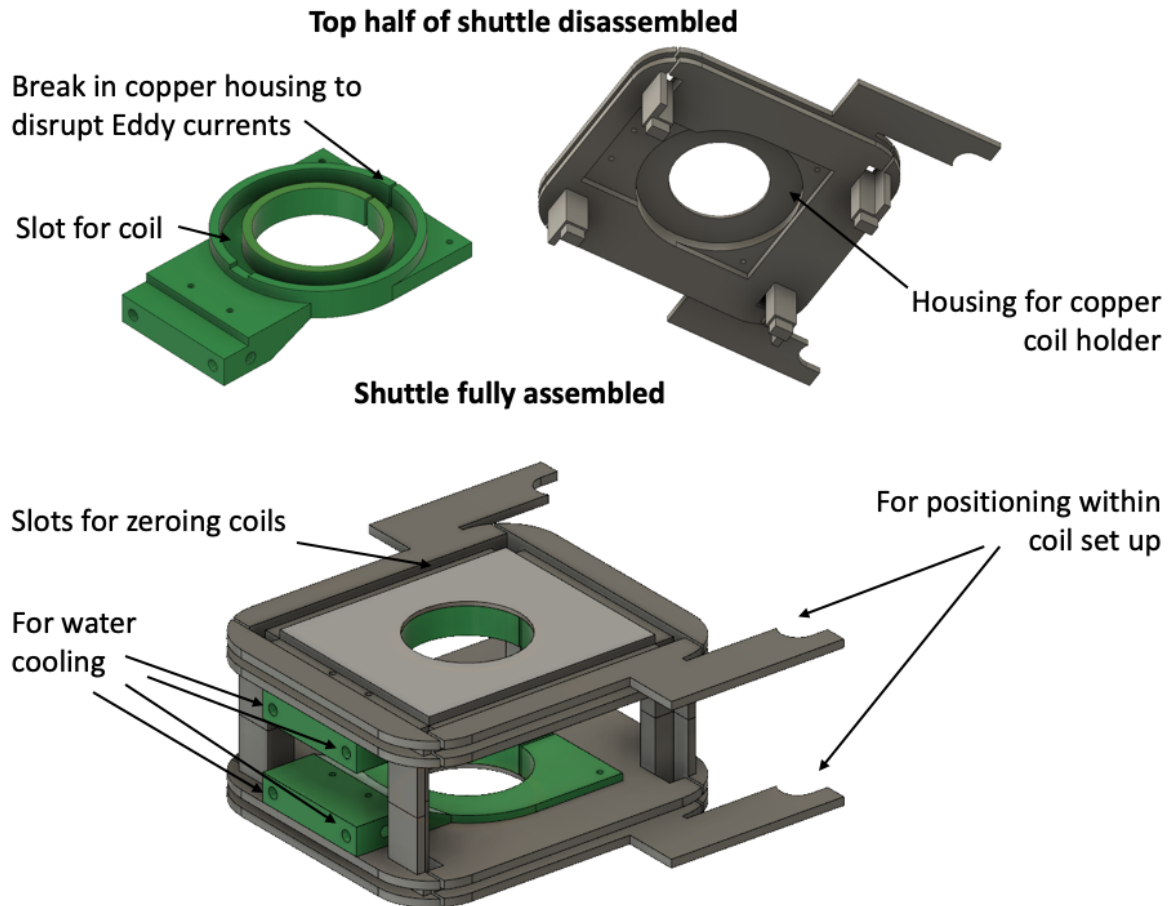
FIGURE 5.2: Shuttle design with annotated features. The green component is the housing for coil to be machined from copper. The green piece attaches to the grey piece, which is to be 3D printed from plastic.

The key features of this shuttle are:

- It includes space for the zeroing coils which are currently on the experiment and explained in Ref. [27].

- The coils are now much closer to the atoms so the current required to achieve the same magnetic fields is reduced thus reducing the load on the BEC coils. The largest magnetic field gradient required in the BEC creation sequence is 145G/cm during the microwave evaporation step, and on the present set up, a current of about 70 amps and average voltage of 34V is required. With the shuttle, the large BEC coils are not needed for this step, and theoretically, only a current of 28.7 A is required with 130 W of power dissipated for 150 G/cm magnetic field gradient (see Appendix for graphs and calculations). This reduction in

power reduces the likelihood of any heat damage occurring.

- In an attempt to mitigate any corrosion, the housing for the shuttle coils is machined from aluminium which will be water cooled (green component in Fig. 5.2). The thermal contact with the housing will also reduce the chance of heat damage occurring.
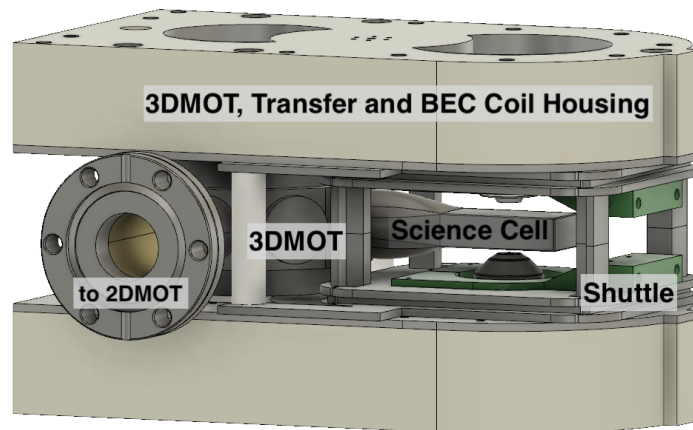

FIGURE 5.3: Shuttle design in existing set up. BEC coils are in the coil housing directly above and below the Science Cell.

The outlook for the experimental set up is good with a fresh vacuum and new coil design, which should reduce the number of times the experiment is out of action every year, along with the newly implemented optical box trap. The experimental apparatus is nearly at a point where the experiment to look for superfluid fountain effect in a BEC could be carried out. The trap depth of the green sheet is the limiting factor as thermal atoms play a crucial role in the superfluid fountain effect and at the moment the green sheet cannot hold onto them. Fixing this is an engineering problem to optimise the fibre coupling and to maximise the power of the green light which the active stabilisation feedback can cope with. After that is optimised, performing a thermal cloud transport experiment similar to the condensate transport experiment I carried out would be an appropriate next step. This would test how (and if) the thermal cloud is transported in the dumbbell configuration.

Going beyond simply looking for the superfluid fountain effect, exploring how the geometry of the channel effects the transport would be interesting. One could see if there is a width

at which point the net flow is no longer from cold to hot but the other direction. We could also try to force the system close to the hydrodynamic regime by changing the geometry of the channel to have corners so a longer channel can fit between the two reservoirs. Also, changing the difference between the condensate fractions in each reservoir to see if there is a relationship between that and the transport.

As mentioned in the introduction, this research was also intended to provide general insight into BEC transport out of thermal equilibrium with the potential application in developing a heat engine. Unfortunately, no results in this thesis were able to provide that insight, but continuing this work is still valuable for this development.
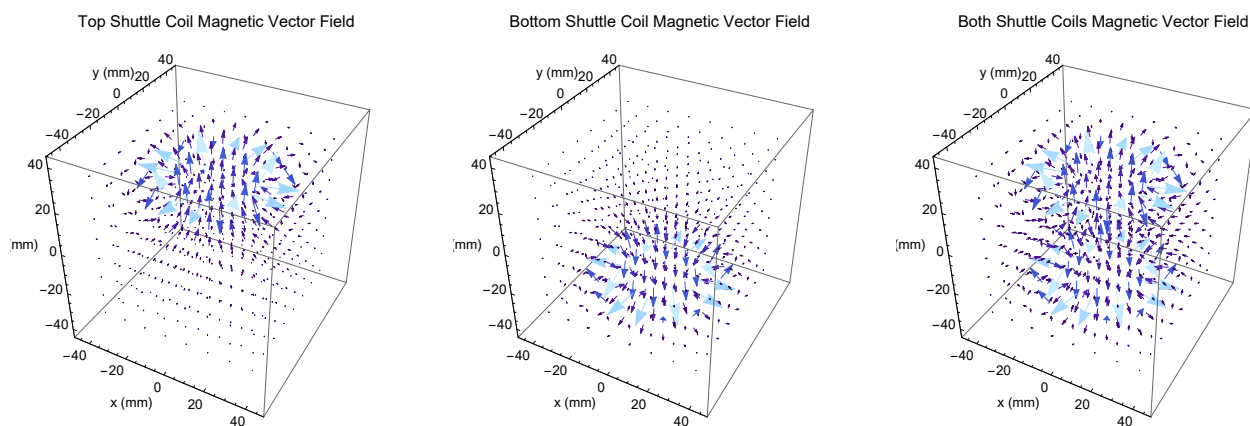
A

An Appendix

FIGURE A.1: Magnetic field from coils

Shuttle Coils Parameter

Inner radius of the top & bottom coils (m)

In[•]:= `innerTopCoilRadius = 0.023; innerBottomCoilRadius = innerTopCoilRadius;`

Outer radius of the top & bottom coils (m)

In[•]:= `outterTopCoilRadius = 0.03; outterBottomCoilRadius = outterTopCoilRadius;`

Average radius of coils (m) - for theoretical check

In[•]:= `averageCoilRadius = (outterTopCoilRadius + innerTopCoilRadius) / 2;`

Number of turns top & bottom coils = (Rad_o - Rad_i)/1.524E-4

In[•]:= `numberTurnsTopCoilManual = 32; numberTurnsBottomCoil = numberTurnsTopCoil;`

In[•]:= `numberTurnsTopCoil = Floor[(outterTopCoilRadius - innerTopCoilRadius) / (1.524 * 10^-4)]; numberTurnsBottomCoil = numberTurnsTopCoil`

Out[•]= `45`

Vertical separation of the Shuttle coils (m)

In[•]:= `coilsVerticalSeperation = 0.033 + 0.006 + 0.00635; topCoilPosition = coilsVerticalSeperation / 2; bottomCoilPosition = -coilsVerticalSeperation / 2;`

Coils current rating (A)

In[•]:= `coilCurrentMaximum = 30; coilCurrentMinimum = -30;`

Shuttle coil current uncertainty (A)

In[•]:= `coilCurrentUncertatinty = 0.5;`

In[•]:= `(* topCoilCurrent=21;bottomCoilCurrent = topCoilCurrent; *)`

Atoms Position Relative to Shuttle Coils Center

In[•]:= `BECoffsetPosition = 0;`

Goals

Vertical magnetic field gradient (G/cm)

In[•]:= `verticalMagneticFieldGradientGoal = -160;`

Horizontal magnetic field gradient (G/cm)

In[•]:= `horizontalMagneticFieldGradientGoal = 0;`

FIGURE A.2: Shuttle coil parameters

Power Dissipation

Power equation

```
In[ ]:= P[R_, I_] := R * I^2;
```

Resistance equation

```
In[ ]:= R[ρ_, L_, A_] := ρ * L / A;
```

Variables

Vertical magnetic field gradient (G/cm)

```
In[ ]:= verticalMagneticFieldGradientGoal = 150;
```

Calculate the required current for the desired magnetic field gradient (A)

```
In[ ]:= requiredCurrent = verticalMagneticFieldGradientGoal / Round[Abs[ShuttleBothDerivedZMagneticFieldGradient[1, -1, BECoffsetPosition]], 0.01]
Out[ ]= 28.7356
```

Copper reistivity (Ohm*m)

```
In[ ]:= copperResistivity = 1.7 * 10^-8;
```

Approximate length of wire (using average diameter, so it will underestimate it by a bit) [m]

```
In[ ]:= length = numberTurnsTopCoil * 2 * averageCoilRadius * Pi
Out[ ]= 7.4927
```

Cross sectional area of 6.35mm coil with width of 127 micrometers (m^2)

```
In[ ]:= crossSectionalArea = 6.35 * 10^-3 * 127 * 10^-6
Out[ ]= 8.0645 × 10^-7
```

Power dissipated (W)

```
In[ ]:= power = P[R[copperResistivity, length, crossSectionalArea], requiredCurrent]
Out[ ]= 130.422
```

```
In[ ]:=
```

FIGURE A.3: Power dissipation from coils

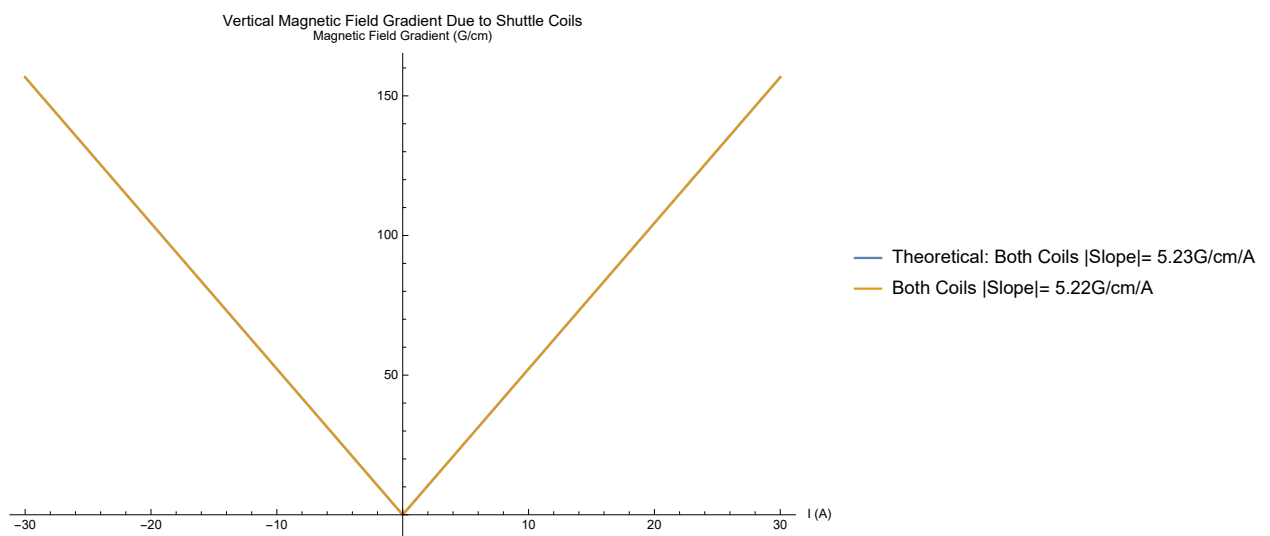FIGURE A.4: Vertical magnetic field gradient

```matlab
1     % Oscilation frequency calculation with uncertainties (Unc)
2 -   N = 1.15e6; %number of atoms - should be 1.2e6 by unc
3 -   NUnc = 9e4;
4 -   u = 1.6605e-27; %amu to kg
5 -   m = 86.9*u; %[kg] Rubidium 87 mass
6 -   wz = 58*(2*pi); % [Hz] Vertical trapping frequency
7 -   wzUnc = 3*(2*pi);
8 -   rad = 35e-6; %[m] radius of dumbbell reservoir
9 -   l = 12e-6; %[m] length of channel
10 -  w = 10e-6; %[m] width of channel
11 -  A = 2*pi*(rad)^2+l*w; %[m^2] calcuated are of dumbbell
12 -  hbar = 1.055e-34; %[Js]
13 -  a0 = 5.29e-11; %[m]
14 -  as = 99*a0; %[m] s-wave scattering length of rubidium
15 -  g = 4*pi*hbar^2*as/m; %from GPE
16 -  mu = 1/2*(3*N*g*(m*wz^2)^(1/2)/(2*A))^(2/3) %chemcial potential
17 -  muUnc = mu*2*sqrt((NUnc/N)^2 + (wzUnc/wz)^2)/3
18 -  c = sqrt(mu/m) %[m/s] speed of sound
19 -  cUnc = c*(1/2)*(muUnc/mu)
20 -  lzcalc = sqrt(2*mu/(m*wz^2)) %Thomas-Fermi radius
21 -  lzcalcUnc = lzcalc*(1/2)*sqrt((muUnc/mu)^2+(2*wzUnc/wz)^2)
22 -  S = w*2*lzcalc %[m^2]
23 -  SUnc = w*2*lzcalcUnc
24 -  V = pi*rad^2*2*lzcalc %[m]^3 Volume of one reservoir
25 -  VUnc = pi*rad^2*2*lzcalcUnc
26 -  delta = 2.14*sqrt(S) % [m] end correction
27 -  deltaUnc = delta*(1/2)*SUnc/S
28 -  omega = c*(S./(l+delta)*2/V).^(1/2) %angular frequency
29    % the following are just breaking down the uncertainty calculation:
30 -  tau = sqrt((l*VUnc)^2 + (V*delta*sqrt((VUnc/V)^2+(deltaUnc/delta)^2))^2);
31 -  gamma = (S/(V*(l+delta)))*sqrt((SUnc/S)^2 + (tau/(V*(l+delta)))^2);
32 -  phi = 2*S/(V*(l+delta))*(1/2)*tau;
33 -  omegaUnc = omega*sqrt((cUnc/c)^2 + (phi/(2*S/(V*(l+delta)))^(1/2))^2)
34    % Oscillation frequency
35 -  f = omega/(2*pi) %in Hz
36 -  fUnc = omegaUnc/(2*pi)
```

FIGURE A.5: Superfluid transport data in box trap uncertainty calculation.

References

[1] J. F. Allen and A. D. Misener. *Flow of Liquid Helium II.* Nature **141**(3558) (1938).

[2] M. H. Anderson, J. R. Ensher, M. R. Matthews, C. E. Wieman, and E. A. Cornell. *Observation of Bose-Einstein condensation in a dilute atomic vapor.* Science **269**(5221), 198 (1995).

[3] K. Davis, M. Mewes, M. Andrews, N. van Druten, D. Durfee, D. Kurn, and W. Ketterle. *Bose-Einstein condensation in a gas of sodium atoms.* Physical review letters **75**(22) (1995).

[4] M. R. Matthews, B. P. Anderson, P. Haljan, D. Hall, C. Wieman, and E. A. Cornell. *Vortices in a Bose-Einstein condensate.* Physical Review Letters **83**(13), 2498 (1999).

[5] C. Raman, M. Köhl, R. Onofrio, D. Durfee, C. Kuklewicz, Z. Hadzibabic, and W. Ketterle. *Evidence for a critical velocity in a Bose-Einstein condensed gas.* Physical Review Letters **83**(13), 2502 (1999).

[6] C. Pethick and H. Smith. *Bose-Einstein condensation in dilute gases / C.J. Pethick, H. Smith.* (Cambridge University Press, Cambridge, UK ; New York, 2008), 2nd ed.

[7] B. Seaman, M. Krämer, D. Anderson, and M. Holland. *Atomtronics: Ultracold-atom analogs of electronic devices.* Physical Review A **75**(2), 023615 (2007).

[8] L. Amico, G. Birkl, M. Boshier, and L.-C. Kwek. *Focus on atomtronics-enabled quantum technologies.* New Journal of Physics **19**(2), 020201 (2017).

[9] J.-P. Brantut, C. Grenier, J. Meineke, D. Stadler, S. Krinner, C. Kollath, T. Esslinger, and A. Georges. *A thermoelectric heat engine with ultracold atoms.* Science **342**(6159), 713 (2013).

[10] J. Wang, J. He, and Y. Ma. *Quantum heat engine based on trapped bose gases: Its maximum efficiency can approach the carnot value at finite power.* arXiv preprint arXiv:1803.03734 (2018).

[11] J. Li, T. Fogarty, S. Campbell, X. Chen, and T. Busch. *An efficient nonlinear feshbach engine.* New Journal of Physics **20**(1), 015005 (2018).

[12] P. Kapitza. *Viscosity of liquid helium below the λ-point.* Nature **141**(3558) (1938).

[13] J. F. Allen and H. Jones. *New Phenomena Connected with Heat Flow in Helium II.* Nature **141**(3562) (1938).

[14] L. Tisza. *Transport phenomena in Helium II.* Nature **141**(3577) (1938).

[15] L. Landau. *Theory of the superfluidity of helium II.* Physical Review **60**(4), 356 (1941).

[16] D. R. Tilley and J. Tilley. *Superfluidity and superconductivity / David R. Tilley, John Tilley.* Graduate student series in physics (Institute of Physics Publishing, Bristol ; Philadelphia, 1990), 3rd ed.. ed.

[17] D. Jin, J. Ensher, M. Matthews, C. Wieman, and E. A. Cornell. *Collective excitations of a Bose-Einstein condensate in a dilute gas.* Physical review letters **77**(3), 420 (1996).

[18] M. Andrews, C. Townsend, H.-J. Miesner, D. Durfee, D. Kurn, and W. Ketterle. *Observation of interference between two Bose condensates.* Science **275**(5300), 637 (1997).

[19] M. T. Reeves. *Quantum Analogues of Two-Dimensional Classical Turbulence.* Ph.D. thesis, University of Otago (2017).

[20] S. Eckel, J. G. Lee, F. Jendrzejewski, C. J. Lobb, G. K. Campbell, and W. T. Hill. *Contact resistance and phase slips in mesoscopic superfluid-atom transport.* Phys. Rev. A **93**, 063619 (2016). URL https://link.aps.org/doi/10.1103/PhysRevA.93.063619.

[21] G. Gauthier, S. S. Szigeti, M. T. Reeves, M. Baker, T. A. Bell, H. Rubinsztein-Dunlop, M. J. Davis, and T. W. Neely. *An atomtronic oscillator circuit for quantum gases.* arXiv preprint arXiv:1903.04086 (2019).

[22] M. Albiez, R. Gati, J. Fölling, S. Hunsmann, M. Cristiani, and M. K. Oberthaler. *Direct observation of tunneling and nonlinear self-trapping in a single bosonic Josephson junction.* Physical review letters **95**(1), 010402 (2005).

[23] T. Karpiuk, B. Grémaud, C. Miniatura, and M. Gajda. *Superfluid fountain effect in a Bose-Einstein condensate.* Phys. Rev. A **86**, 033619 (2012). URL https://link.aps.org/doi/10.1103/PhysRevA.86.033619.

[24] D. J. Papoular, G. Ferrari, L. P. Pitaevskii, and S. Stringari. *Increasing quantum degeneracy by heating a superfluid.* Phys. Rev. Lett. **109**, 084501 (2012). URL https://link.aps.org/doi/10.1103/PhysRevLett.109.084501.

[25] D. Husmann, M. Lebrat, S. Häusler, J.-P. Brantut, L. Corman, and T. Esslinger. *Breakdown of the Wiedemann–Franz law in a unitary Fermi gas.* Proceedings of the National Academy of Sciences **115**(34), 8563 (2018). https://www.pnas.org/content/115/34/8563.full.pdf, URL https://www.pnas.org/content/115/34/8563.

[26] G. Gauthier, I. Lenton, M. Baker, M. Davis, H. Rubinsztein-Dunlop, and T. Neely. *Direct imaging of a digital-micromirror device for configurable microscopic optical potentials.* Optica **3**(10) (2016). URL http://search.proquest.com/docview/2080734817/.

[27] G. Gauthier. *Transport and Turbulence in Quasi-Uniform and Versatile Bose-Einstein Condensates.* Ph.D. thesis, Shool of Mathematics and Physics, The University of Queenslad (2018). Unpublished.

[28] J. L. Ville, T. Bienaimé, R. Saint-Jalm, L. Corman, M. Aidelsburger, L. Chomaz, K. Kleinlein, D. Perconte, S. Nascimbène, J. Dalibard, and J. Beugnon. *Loading and*

compression of a single two-dimensional bose gas in an optical accordion. Phys. Rev. A **95**, 013632 (2017). URL `https://link.aps.org/doi/10.1103/PhysRevA.95.013632`.

[29] N. Navon, A. L. Gaunt, R. P. Smith, and Z. Hadzibabic. *Emergence of a turbulent cascade in a quantum gas.* Nature **539**(7627), 72 (2016).

[30] N. M. Parry. *Design, Construction, and Performance towards A Versatile 87Rb & 41K BEC Apparatus.* Master's thesis, School of Mathematics and Physics, The University of Queensland (2015).

[31] Z. L. Newman. *A NEW APPARATUS FOR STUDIES OF QUANTIZED VORTEX DYNAMICS IN DILUTE-GAS BOSE-EINSTEIN CONDENSATES.* Ph.D. thesis, College of Optical Sciences, The University of Arizona (2016).